Final Report

Measuring Radiation Damage from Heavy Energetic Ions in Aluminum

Funded by DOE under **DE-FG02-07ER41472**

M. Kostin (PI), R. Ronningen(PI), Michigan State University
L. Ahle (PI), Lawrence Livermore National Laboratory
T. Gabriel, Scientific Investigation and Development
L. Mansur (PI), K. Leonard, Oak Ridge National Laboratory
N. Mokhov, Fermi National Accelerator Laboratory
K. Niita, Research Organization for Information Science and Technology, Japan

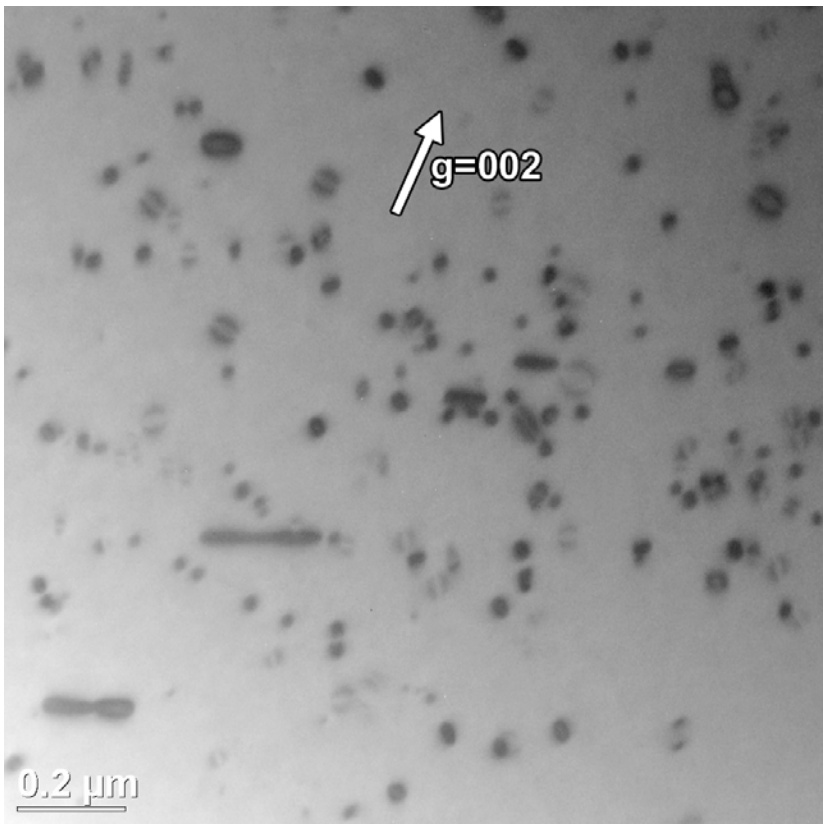

February 2009

Measuring Radiation Damage from Heavy Energetic Ions in Aluminum

DE-FG02-07ER41472

Funding received in k$

	FY 07/08
Michigan State University (M. Kostin, R. Ronningen)	**50**
Oak Ridge National Laboratory (L. Mansur)	**95**
Lawrence Livermore Laboratory (L. Ahle)	**30**
Total	**175**

Abstract

An intense beam of 122 MeV/u (9.3 GeV) ^{76}Ge ions was stopped in aluminum samples at the Coupled Cyclotron Facility at NSCL, MSU. Attempts were made at ORNL to measure changes in material properties by measuring changes in electrical resistivity and microhardness, and by transmission electron microscopy characterization, for defect density caused by radiation damage, as a function of depth and integrated ion flux. These measurements are relevant for estimating damage to components at a rare isotope beam facility.

Introduction

Research with rare ion beams has been recognized by both the nuclear and high energy physics communities as critical to advancing these sciences. However, it has been acknowledged that substantial progress can only be made with a new generation of high-power facilities. The United States is embarking on the design and construction of the next-generation rare isotope beam facility FRIB [1]. This facility will utilize higher beam powers, ≥100 kW. These high power beams will require substantial advances in accelerator and target technology, especially related to materials issues and power handling. Particular areas that need focused attention include radiation damage, material activation, heating, and optimization of rare isotope production. Many materials issues that are encountered in high power accelerators have been discussed by Mansur [2].

Fragmentation is one method used to produce an intense beam of short-lived isotopes. An accelerated heavy ion such as uranium interacts with a target (e.g., Li, Be, or C). During the fragmentation process, the heavy ion beam first impinges on the target where a fraction, say 20%, of the beam is reacted. The fragments thus produced and the rest of the beam pass through magnets comprising a fragmentation pre-separator. In addition to the majority of beam ions, other ions and other fragments are absorbed in the beam dumps. The produced fragments of interest generated in the target continue down the centerline of the pre-separator and are transported to end-stations, where they may be captured and studied, or made to produce other reactions for study.

The impact of the U beam and other ions results in radiation damage to the material of the beam dump and other structural components. This damage leads to degradation of the properties of the material including changes in mechanical properties, dimensional stability and physical properties. Two examples for each of these detrimental effects include embrittlement and hardening, swelling and radiation creep, loss of thermal conductivity and increase in electrical resistivity, respectively. Simulations of damage, giving dose in displacements per atom, dpa, were made for a pre-concept of a Rare Isotope Accelerator water-cooled copper dump [3]. The results showed that 25 displacements per atom would be accumulated per day in beam dump material, resulting in displacement doses of order hundreds of dpa per month. This is a very high dose in terms of previous experience with radiation damage in fission reactors and charged particle accelerator targets, and can be expected to alter substantially all properties of these materials. In addition there is a substantial uncertainty in the level of radiation damage because of approximations made in the calculations.

Background

It may be possible to reduce the level of radiation damage by choosing a better-optimized design. Nonetheless, one would have to rely on simulations done with radiation transport Monte Carlo codes with heavy ion tracking capabilities such as PHITS [4], MARS15 [5-8], MCNPX [9], SRIM [10] and FLUKA[11, 12]. These codes exclude a potentially large additional source of displacement damage. This source of radiation damage has not been fully explored and therefore has not been quantified. It is termed the swift heavy ion

effect. When a charged particle impinges on a solid the particle loses energy in two general classes of interactions. These are electronic stopping and nuclear stopping. The former includes all electronic interactions, such as ionization of target atoms and excitation of lower shell electrons into excited states. The latter describes all nuclear processes including elastic interactions, and all non-elastic nuclear reactions with target atoms, as well as atom-atom interactions at lower energies.

In metallic alloys it has long been accepted that only nuclear stopping can produce displacements of atoms. Electronic stopping is dissipated without producing displacements. This occurs because of the presence of a Fermi sea of electrons, the signature of metallic structures where an electron is not associated with a particular nucleus. In metals charge neutrality is restored quickly after passage of an energetic heavy ion because of the high mobility and essentially unlimited range of electrons in the structure.

The energy delivered as nuclear stopping has been termed the damage energy and has been well established as the component leading to displacements in fission reactor and low energy (MeV range) charged particle irradiations in metals. The vast majority of experimental radiation effects data available today has been obtained from irradiations in these two types of facilities. However, relatively recent experimental work with so called swift heavy ions (GeV range) has shown that more displacements may be produced than can be accounted by nuclear stopping alone in some metals. In these cases the linear energy transfer (LET) of the ion, the energy lost per unit distance, for electronic stopping is typically 10^3 times larger than the LET for nuclear stopping. In some cases it has been found that most displacement damage is actually produced by electronic stopping rather than by nuclear stopping in very high energy ion irradiations [13, 14]. The rough quantitative criterion is that the swift heavy ion effect has been found to be important in producing displacements by electronic stopping in metals where the electronic LET is greater than about 10 to 40 keV/nm, depending on the material. Below this range the displacement damage in metals generally can be accounted for by nuclear stopping.

In insulators and semiconductors, on the other hand, electronic stopping can be important in producing displacements in swift heavy ion irradiations and also in lower energy ion irradiations. The much slower recovery of the electronic structure in ceramics and semiconductors, due to the lower and spatially limited electron mobility, can give rise to longer term charge separation in these materials. This in turn can lead to atoms being energetically pushed off their lattice sites by Coulomb interactions and by radiolysis.

The production of displaced atoms is a complex process, and is best thought of as a number of competing and mutually interacting processes. For example in metals, even in lower energy ion irradiations where displacements are produced only by nuclear stopping, there is a large fraction of the incident ion energy transferred to the electronic structure. This energy component is not entirely innocuous in metals as is usually assumed. In fact, the subsequent dissipation as heat of the energy absorbed in electronic stopping can result in some of the defects produced by displacement damage being recombined (i.e., the mutual annihilation of a vacancy and an interstitial). This process of

annealing of displacement damage by the fraction of ion energy absorbed as electronic stopping also occurs at higher incident ion energies in the GeV range of swift heavy ion irradiation. It thus competes with the increased production of displaced atoms also traceable to the fraction of ion energy absorbed as electronic stopping discussed above [14, 15].

Displacement mechanisms by nuclear stopping are well described by knock-on events. On the other hand the mechanisms by which electronic energy loss leads to atom displacements are not fully established and several ideas have been put forward. The crux of the issue is how to couple or translate efficiently the energy imparted to the electronic system to the atomic system of a metal. One suggested mechanism is the thermal spike model. In principle one mechanism by which the energy in the electronic system can be transferred to the atomic system is by energizing phonons. That a thermal spike occurs in a nuclear collision that displaces atoms was suggested about 50 years ago. The localized spatial region where the atoms are displaced is hot in terms of kinetic energy of atom motion. Corresponding atom energies are well above kT, where k is Boltzmann's constant and T is the local ambient temperature. Until the heat is dissipated, the atomic structure in the region can be in an amorphous state or in a highly defected crystalline state. This idea has been carried over more recently to high energy deposition electronic stopping. If the atomic kinetic energy transmitted by phonon coupling or other processes from the initial high density electronic energy deposition is large enough, then a thermal spike may be triggered by electronic processes alone that create atomic lattice defects, i.e., displaced atoms. An alternative suggestion is the Coulomb explosion model. Here the rapid wholesale stripping of electrons from target atoms during the passage of a swift heavy ion creates a region of positive charge with high repulsive potential energy, which persists for an extremely short time. During this period atoms can be forced from their lattice sites with the consequent creation of vacant lattice sites and displaced interstitial atoms.

As of today, the predictive power of radiation transport codes for the radiation damage caused by heavy energetic ions is insufficient. Moreover, capability to predict the radiation damage in terms of dpa may not be sufficient for successful facility design. It is also critical to know how to associate a certain level of radiation damage with changes in bulk material properties such as hardness, ductility and swelling because the lifetime of the components does depend on the intended use. Whereas the radiation damage may not be a significant concern for a facility component without a structural function, for other components the change in the bulk material properties may be significant enough to lead to a component failure. An example of that might be a failure of a water-cooled beam dump due to the swelling of the material resulting in a reduced water flow. Our capabilities in this area are somewhat less than sufficient due to the lack of experimental data.

The purpose of the present work was to carry out irradiation experiments on aluminum specimens to explore swift heavy ion radiation damage. This work employed an initial beam of ^{76}Ge ions of approximately 9.9 GeV (130 MeV/nucleon). The stopping of 122 MeV/u (9.3 GeV) ^{76}Ge ions in aluminum is shown in Figure 2, as calculated using SRIM.

The energy of 122 MeV/u is reached by the ^{76}Ge ions after the initial beam passes through a vacuum window and air at the experimental setup.

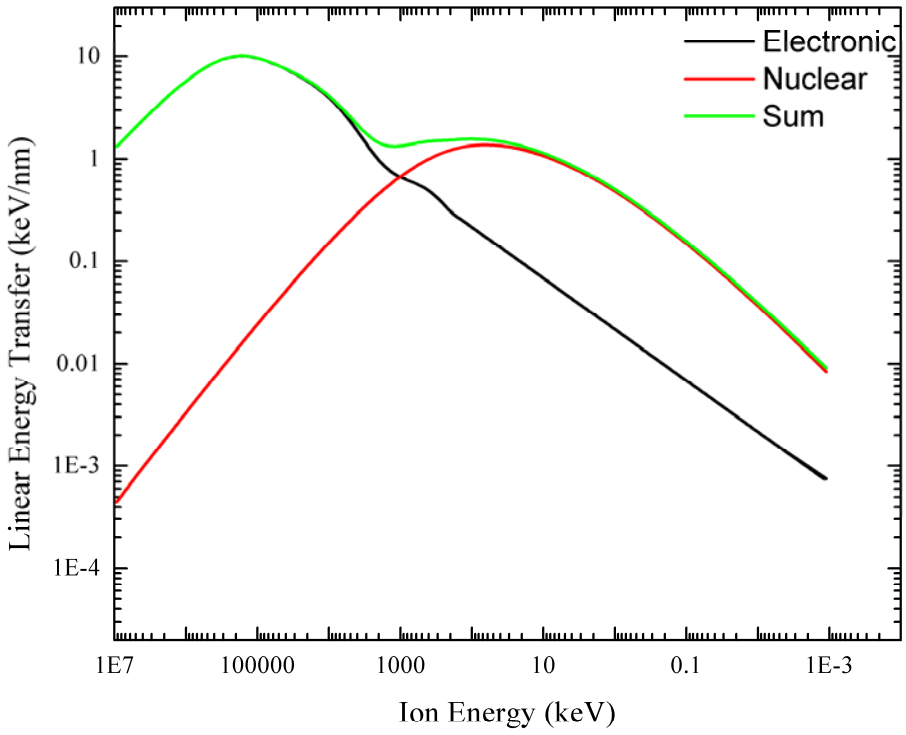

Figure 1: Linear energy transfer ("LET" or "Stopping Power"), the energy lost per unit path length, is shown as a function of energy for a beam of ^{76}Ge ions stopping in aluminum (ρ = 2.70 g/cm^3). The electronic and nuclear components of LET are shown as is their sum.

These ions are calculated to have an initial LET of 1.32 keV/nm and to reach approximately 10 keV/nm in the early stage of slowing down. These LET values are in the range for possible swift heavy ion damage from electronic energy deposition. Characterizations of the irradiated specimens by several measurement techniques were then obtained to measure the extent of radiation damage. The measurements included transmission electron microscopy, electrical resistivity and hardness.

Previous Experiments

The radiation damage has been relatively well studied for neutron and proton irradiation on copper for instance [16]. Figure 2 shows how the defect density increases up to ~1 dpa and then the density saturates. Not all the radiation effects saturate. The swelling of materials continues to increase and the ductility continues to drop until unacceptable levels are reached. It should be noted, that the material damage caused by heavy ions may differ from that by neutrons. Neutrons produce more uniform damage distribution whereas heavy ions tend to produce more localized regions of defects. Chemistry change

in materials by transmutation caused by heavy ions may differ from that by neutrons. It is also not clear whether the saturation effect observed in neutron irradiation exists at very high doses for heavy ion irradiation.

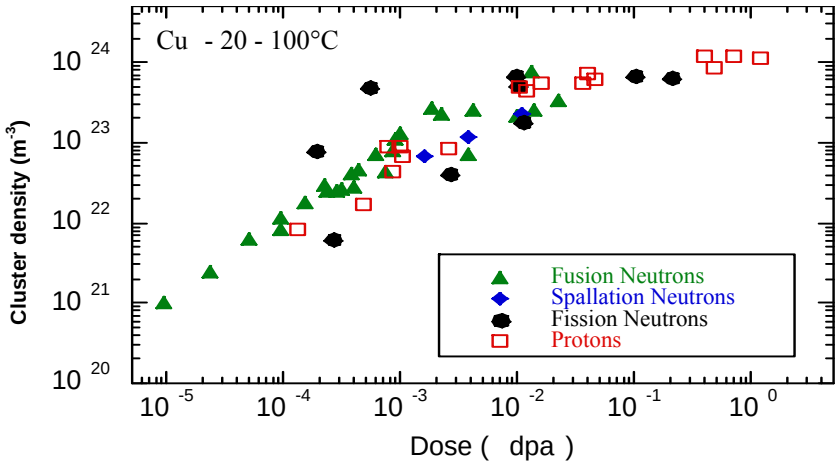

Figure 2: Plot of observed material damage as a function of dpa for neutrons and protons on copper [16].

Results from an earlier radiation damage experiment were reported in the Final Report to DOE on Development of a Concept for High Power Beam Dumps and Catchers, and the Pre-separator Area Layout for Fragment Separators for RIA (DE-FG02-04ER41313) [17]. The collaboration in this project (several members are also members of the present project) irradiated Be, Al, Cu and Ti samples with ~5 MeV/u uranium ions at the ATLAS facility at ANL. Due to lack of funds to complete analyses only preliminary results were obtained. A set of three aluminum samples (6061 T5) irradiated to 5.0×10^{-5} dpa were analyzed using TEM. Several aluminum samples were also measured for hardness changes. From the analyses that could be performed it appeared that damage was peaked near the end of the range of the uranium ions, qualitatively agreeing with the model calculations. It was pointed out that choice of alloy could have dramatic impact as to the effect of radiation damage from heavy ion beams.

Review of the Experiment

The experiment described in this report had two stages – design and irradiation of specimens, and material analysis. The first stage, design and irradiation, was carried out at the National Superconducting Cyclotron Laboratory, NSCL, Michigan State University with the irradiation performed at the Coupled Cyclotron Facility, CCF. The beam energies and species available at CCF are somewhat similar to those expected at a next generation facility such as FRIB [1]. That makes NSCL a good place to study the radiation damage because the results of the experiment would be directly applicable to the design of FRIB. The beam used in our experiment was ^{76}Ge at 130 MeV/nucleon. Two stacks of specimens of high purity aluminum were irradiated at two damage levels of approximately 0.0022 dpa and 0.016 dpa. The damage was predicted with the PHITS code. Low-levels of induced residual activities in the specimens (measured exposure rates

were below 15 mR/hr at 30 cm, 10 minutes after irradiation) allowed us to conduct the second part of the experiment, the material analysis, at the Low Activation Materials Design and Analysis (LAMDA) facility at ORNL. The material analysis included measurements of the electrical resistivity and micro-hardness of aluminum at various depths, and analysis of microstructure with transmission electron microscopy, TEM.

Specimen design

Due to high beam intensities and high charge state of heavy ions at the future rare isotope facilities one might expect that the power density deposited by the beams in beam line components intercepting the beams will be very significant. One way to mitigate such extremely high power densities is to use light materials for such devices thus allowing more volume for the power to be deposited in. One can speculate that a radiation resistant aluminum alloy would be a good choice. For the purpose of this experiment a pure material is better, however. It is much harder to interpret results of material analysis for alloys because of impurities that cause defects created by the radiation to recombine. Precipitation reactions also may be induced in alloys by irradiation. Therefore, after careful consideration, we decided to construct our irradiation specimens from high purity aluminum.

Availability of experiment beam time would not allow us to achieve any significant radiation damage in the specimens, and the expected changes in the bulk properties and microstructure were quite small. The design of the irradiation specimens was driven by this expectation. Our goal was to determine the effects caused by the radiation at various depths, and a stack of foils orthogonal to the beam direction was preferred over a solid specimen. The use of a solid target would require cutting the target after irradiation to prepare material samples for analysis. Since aluminum is a soft material, such cutting would impose a considerable risk for introducing mechanical damage by bending the material and by the machining itself. Such mechanical damage can be a significant background to low levels of the radiation damage in our experiment. The use of the foil stack, on the other hand, eliminates the cutting and thus minimizes chances to introduce unnecessary mechanical damage.

The thickness of the aluminum foils must be small enough to provide required spatial resolution. On the other hand, the foils must be thick enough to maintain rigidity. A 0.25 mm – thick aluminum foil was chosen after a careful consideration. The other dimensions of the foils are driven by spatial constrains of a rig for measurement of the electrical resistivity. Figure 3 shows one foil as it was designed and fabricated with an electric discharge machine. Foils with a required purity of 99.999 % (high purity grade) and 0.25 mm thicknesses were purchased from the company Goodfellow [18].

A total of 30 foils was used to construct one irradiation specimen, summing up to 7.5 mm in aluminum thickness. This thickness exceeds the stopping range of ^{76}Ge at 130 MeV/nucleon. The stopping range was found to be approximately 4.8 mm as calculated with SRIM. The stopping range was also confirmed with PHITS and MARS15.

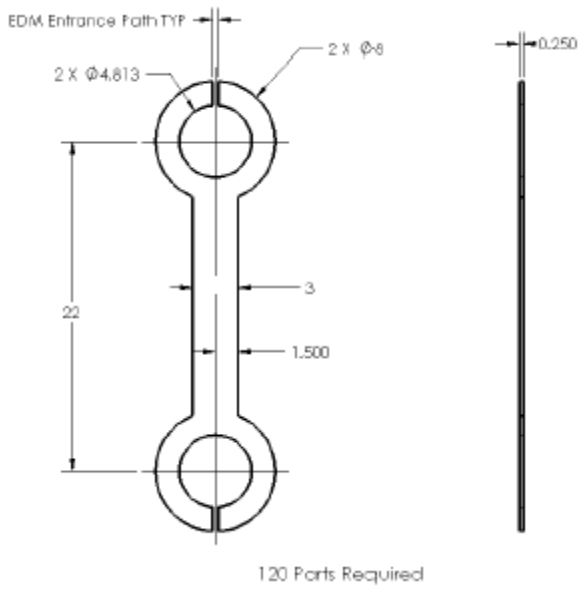

Figure 3: Foil dimensions shown in mm. Round parts at the ends serve to attach the foil to a holder.

Due to the deposited beam power, the temperature of the specimens during irradiation was expected to exceed room temperature. It is important to understand that under these conditions we do not see the original, total damage caused by the ions but only some remaining fraction. The melting point of aluminum is 660^{o}C, which is relatively low, and room temperature is approximately one third of that in terms of absolute temperature. The defects in aluminum would move and partially anneal at even room temperature. Heating of the material over the room temperature would lead to conditions at which a significant portion of the defects may disappear. Therefore, it would be desirable to keep the temperature of the specimens during irradiation as low as possible. Previous measurements of the radiation damage conducted at HFIR at ORNL [19] suggested that a comfortable temperature for this sort of experiment is 70^{o}C and it should not exceed 100^{o}C. At 150^{o}C, the defect density caused by the radiation will significantly deteriorate. A thermal analysis of the specimens showed that active cooling would be required to keep the temperature down and thus to achieve desired damage within a reasonable time. A number of cooling schemes were considered. But given the time constraints, we adopted one that was least uncertain – a specimen with separated foils cooled by an air flow.

The thermal analysis of the specimens required input from radiation transport codes in form of the energy deposition. The energy deposition was calculated with PHITS and MARS15. The calculations were done for a beam of ^{86}Kr at 140 MeV/nucleon with a current of 20 pnA. The total power deposited in a target is 200 W as calculated with the PHITS code and 230 W as calculated with MARS15. Associated power density distributions are shown in Figure 4 and Figure 5. That beam was not available at the time of the experiment, however. Instead, a beam of ^{76}Ge at 130 MeV/nucleon was used.

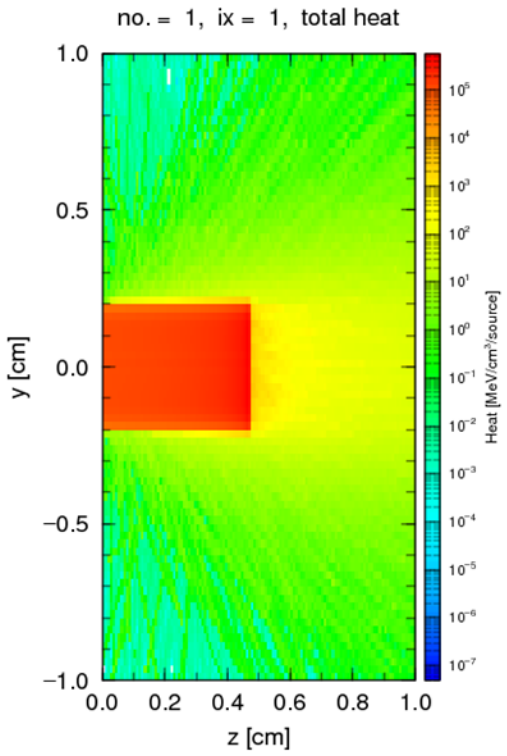

Figure 4: Energy deposition in aluminum as calculated with PHITS

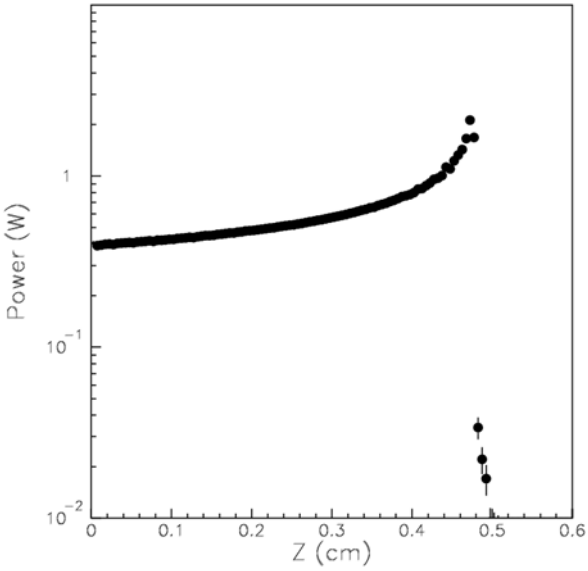

Figure 5: Power deposition in a central part of aluminum target as calculated with MARS15. The bin size is 0.05 mm.

Figure 6 shows calculated *estimates* of the steady-state foil temperature for various beam powers and cooling air velocities. The beam was assumed to be 3 mm in diameter with a flat distribution. Temperature of the air was 65^{o}C. Only distributions for the foil at the Bragg peak are shown, where the deposited power and thus the generated temperature is the greatest among the foils.

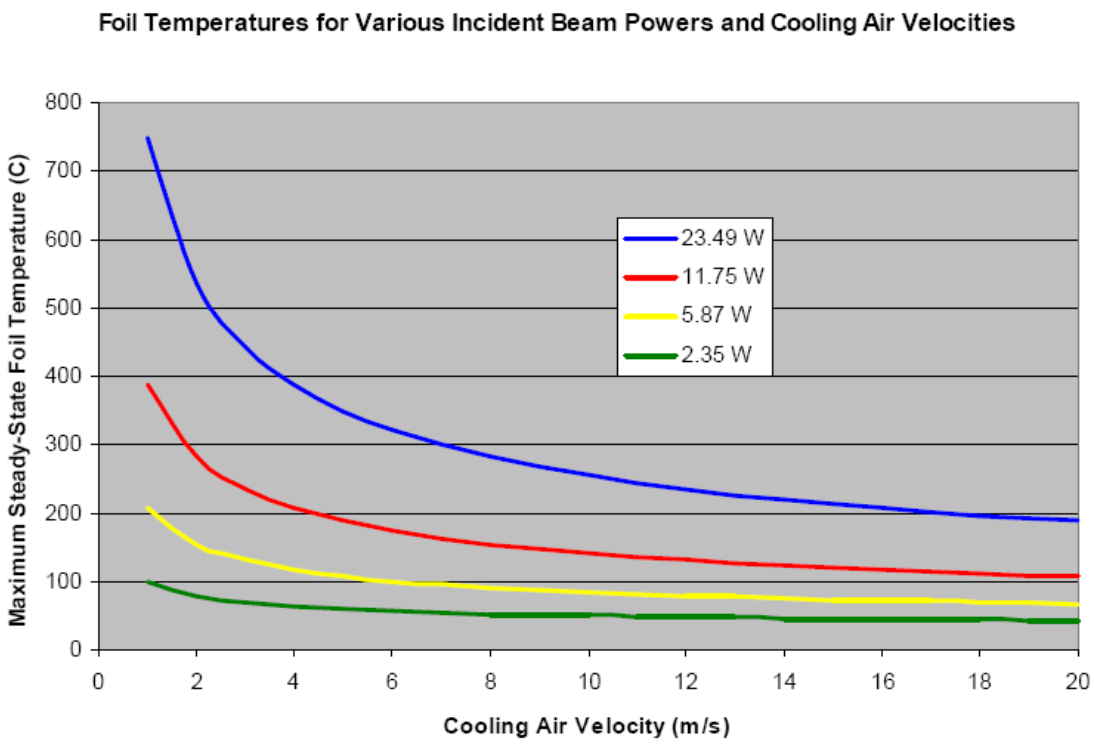

Figure 6: Steady-state foil temperatures for various incident beam powers and cooling air velocities.

An objective was to keep the specimen temperature below 100ºC. Relying solely on air-cooling, this becomes feasible with an incident beam power of about 5 W or less. It is obvious from the above figure that as the velocity of the cooling air is increased, the cooling effectiveness also increases. However, the convection phenomenon is very dependent on surface area. Thus, if the size of each foil can be increased, then the amount of cooling will increase accordingly, decreasing the steady-state temperature. Increasing the foil spacing would also be beneficial to allow more cooling air to pass through each gap between neighboring foils. Calculations showed that a 1 mm wide gap between neighboring foils is sufficient to maintain the desired temperature at foil dimensions outlined above, a beam power of 2.35 W and an air flow of 2 m/s. All of the values presented here are only *estimates*. The empirical correlations that these calculations have been based on are known to introduce errors as large as ± 25%.

Photographic images of fabricated specimens are shown below in Figure 7 and Figure 8. The foils were mounted on copper rods and attached to copper frames. Separation between neighboring foils was provided with 1 mm -thick copper washers.

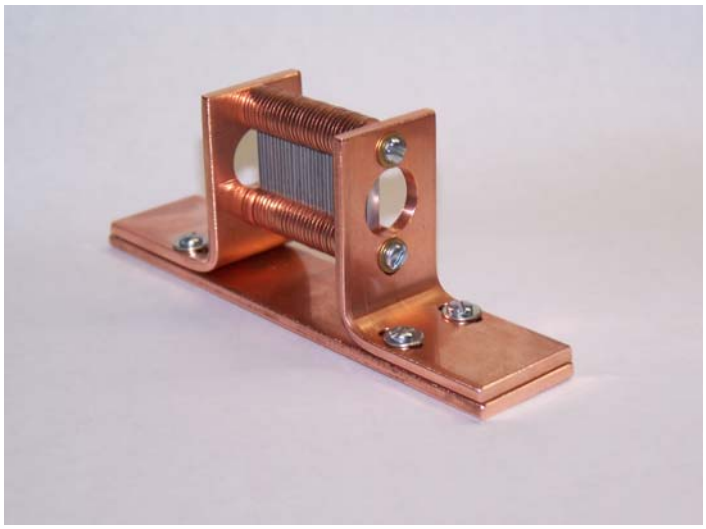

Figure 7: One of the irradiation target assemblies.

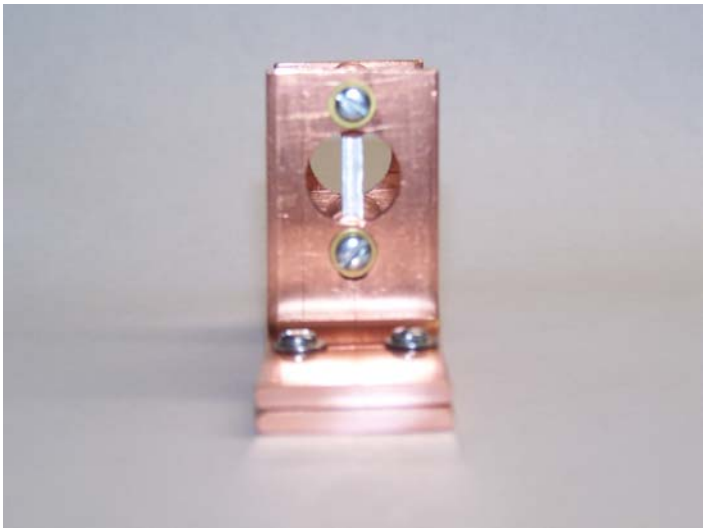

Figure 8: Front view of one of the irradiation target assemblies.

Specimen preparation (annealing)

Defects left in aluminum after fabrication and processing must be annealed. The annealing was done in a vacuum furnace at NSCL in order to avoid excessive oxidation of the foils. Experiments conducted at ORNL [20] showed that sufficient annealing conditions for pure aluminum were to keep it at a temperature of 350^{o}C for one hour. In our case, heating up and cooling down of the specimens placed in the vacuum furnace was done by radiation-heating and radiation-cooling. Therefore, it took approximately 12 hours to complete an annealing cycle. The temperature of a specimen during the annealing was controlled by a thermocouple touching the specimen as shown in Figure 9. There were three irradiation specimens prepared for the experiment. Two of them were irradiated and one was used as a control sample to study the background.

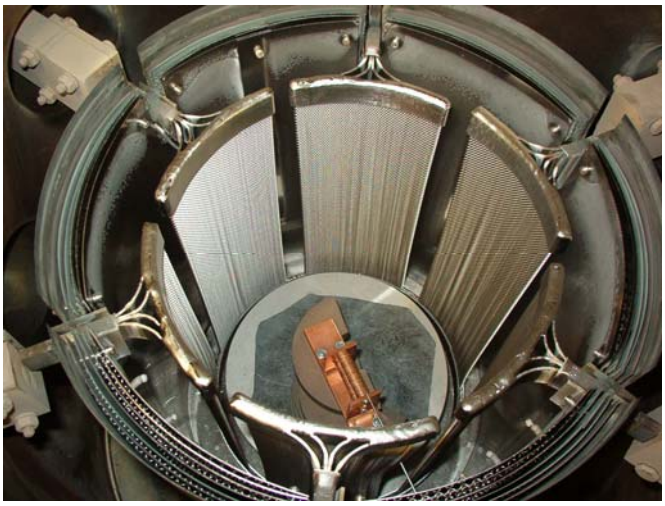

Figure 9: Irradiation specimens with attached thermocouple were placed in the vacuum furnace.

Calculation of Required Beam Time

The beam power used in the experiment was driven by the target cooling requirements. For a 3mm flat beam, the maximum beam intensity is 0.2 pnA, that is 1% of the maximum beam power available at the facility. The radiation damage in pure aluminum caused by ^{76}Ge beam was calculated with PHITS and is shown in Figure 10. The calculations was done for a 6mm beam, therefore some renormalization is needed to be able to use the results for the 3mm beam. The calculations do not take into account the damage caused by the electrons, only the nuclear contribution is taken into account. The predicted damage is $\approx 10^{-16}$ dpa/projectile. This translates into the beam time required to achieve doses of 0.001 dpa and 0.01 dpa of approximately 1 h and 10 h respectively.

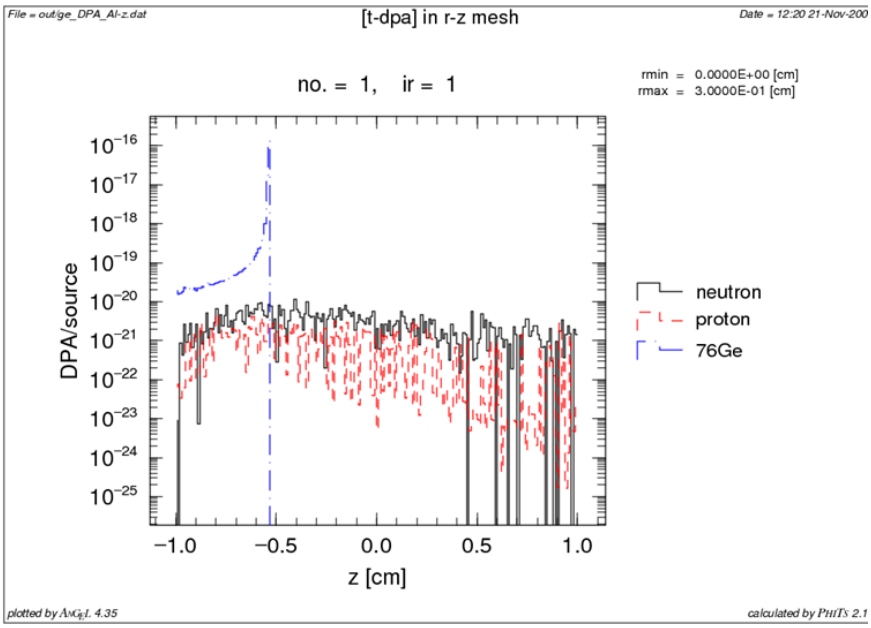

Figure 10: Radiation damage in term of dpa calculated with the PHITS code.

Specimen irradiation

Irradiations were done at the Single Event Effects Test Facility (SEETF) at NSCL [21]. A schematic view of the Coupled Cyclotron Facility at NSCL and the location of the SEETF beam line is shown in Figure 11.

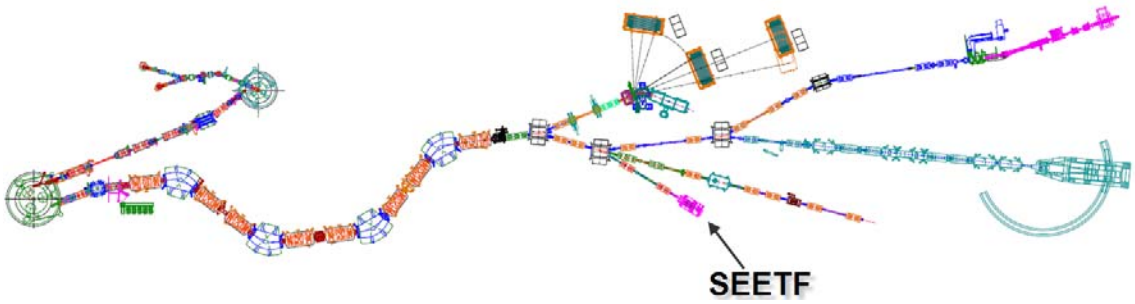

Figure 11: Schematic view of the Coupled Cyclotron Facility at NSCL. The location of the SEETF beam line is shown.

Figure 12 shows the SEEFT irradiation station. The station is equipped with a sample mounting platform (this can move up-down and left-right with respect to the beam), a graphite beam dump, two lasers with beams crossing at the center of the particle beam, a dimension-calibrated scintillator screen that is used to measure the beam position and size. The vacuum chamber was equipped with a 75 μm Zr beam-exit window, a Faraday cup, a Parallel Plate Avalanche Counter (PPAC) system for beam profile measurements at low intensities. The window and air between the vacuum chamber and the sample mounting platform reduce the beam energy of ^{76}Ge from 130 MeV/nucleon to 122 MeV/nucleon, as calculated using SRIM. The total beam intensity can be measured with a Faraday cup inserted into the beam. The beam profile can be measured with the PPAC but only at very low beam intensities. The beam profile is known to change while the intensity increases, introducing uncertainties at high as 50% [22]. In addition, there is a remote video camera that allows one to observe the target mounting platform. We also installed a portable air conditioner to cool down the specimens. The velocity and temperature of air from the air conditioner were measured and found to be ≈1 m/s and 12^{o}C respectively at the specimen position. Note that these parameters are different from those used in the specimen design therefore new thermal analysis was required. The thermal analysis carried out with the above parameters showed that the peak steady-state foil temperature would be 80-100^{o}C.

Figure 13 and Figure 14 show the table with a target mounted on it in greater details. Since the PPAC cannot be used at high intensities, an alternative method was used to monitor the beam position. Laboratory-grade glass slides that are used with optical microscopes are known to darken while irradiated. We used this feature for our benefit. In the beginning and end of each irradiation we monitored the beam position by attaching pieces of glass slides to the targets and irradiating them. At the beam intensities used it only takes a few minutes for the glass to darken. The process of the darkening was observed with the remote camera.

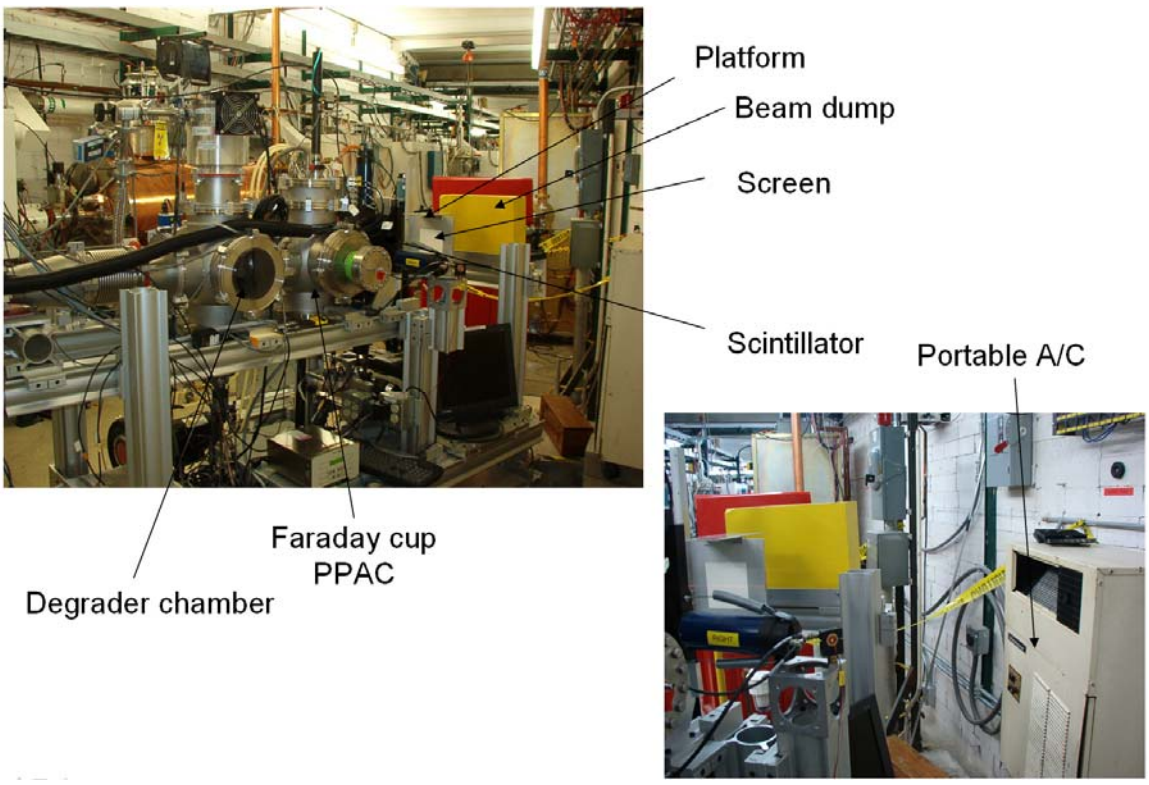

Figure 12: SEETF irradiation station.

The front of a target can be easily aligned with the laser beams. The laser beams are not parallel to the particle beam however. Since the target is quite long we had to take care of the alignment of the back of the target. We did that with an optical telescope placed behind the graphite beam dump. When a target was mounted on the table, the beam dump was removed and the position and orientation of the target were measured and monitored with the telescope. The dump was then replaced.

The total beam intensity was measured with the Faraday cup. In order to ensure that the beam intensity did not change significantly during the irradiation, we also measured the electric current flowing from the target induced by stopped ions. The targets were electrically insulated from the mounting table.

We found it more convenient to use a larger beam spot. The beam can move slightly during irradiation, and since there are no means to monitor for that, the uniformity of the beam within a 3 mm spot can be achieved by using a larger beam spot. The beam spot used in the experiment was approximately 8 mm in diameter, as measured on the dark areas of the glass slides. The beam profile is bell shaped, and an 8-mm beam provides a 3 mm spot with more or less flat beam distribution. In order to keep the beam intensity in the central part of the beam close to 0.2 pnA, the total beam intensity was increased to 0.4 pnA. Since the cooling of the foils in the model that we used to calculate the foil temperature depends only on the number of beam particles per area, and that is similar in an 8 mm 0.4 pnA beam and in a 3 mm 0.2 pnA beam, the foil temperature was not expected to change compared to the calculations.

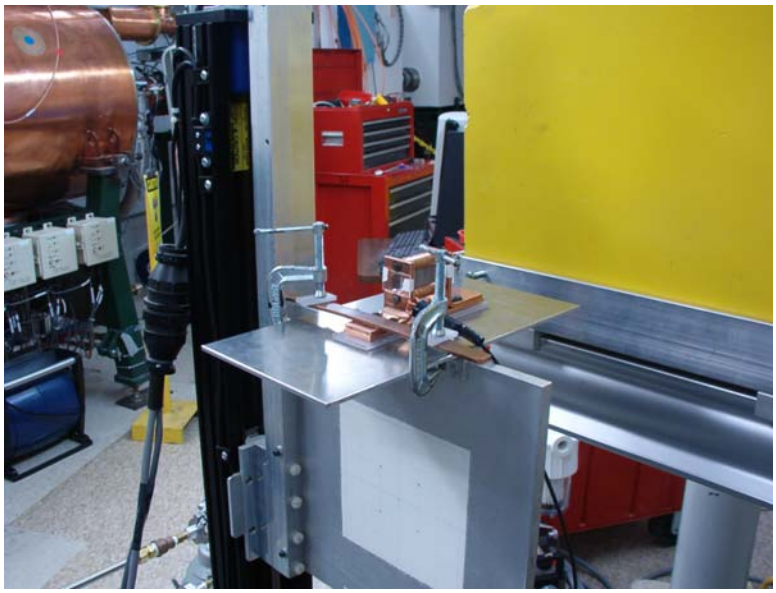

Figure 13: Irradiation target assembly mounted on the platform.

Figure 14: Irradiation target assembly with attached pieces of laboratory glass slides.

Two irradiation runs were conducted, of 1.25 h and 9.25 h duration, achieving approximately 0.0022 dpa and 0.016 dpa respectively. The residual activation exposure rate was measured 10 minutes after the irradiation and was found to be below 15 mR/hr at 30 cm in both cases.

Post-Irradiation Activation Analysis

To meet US Nuclear Regulatory and Department of Transportation regulations for shipping the irradiated samples to ORNL, photon spectra from radioactivity in the two samples were collected using an energy, efficiency-calibrated high-purity Ge photon detector.

Figure 15 and Figure 16 show the photon spectra (overlapped) from the two samples. The activities in the spectra were isotope-identified using standard gamma spectroscopy techniques.

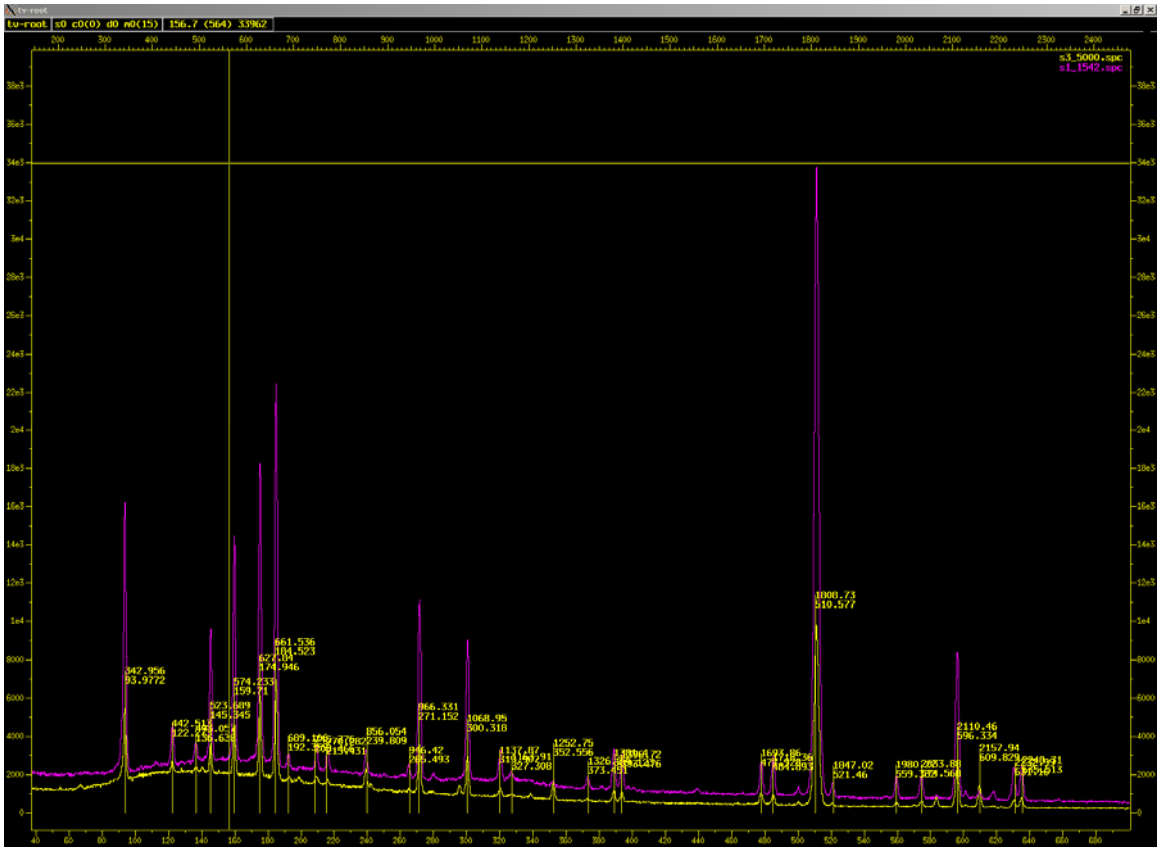

Figure 15: Lower-energy (<700 keV) photon energy spectra from Sample 1 (low-dose run) and Sample 3 (high dose run) are compared. At each peak marker, displayed by the vertical lines, the upper number is the peak centroid in units of channels and the lower number is the photon energy in units of keV as calculated using the centroid value.

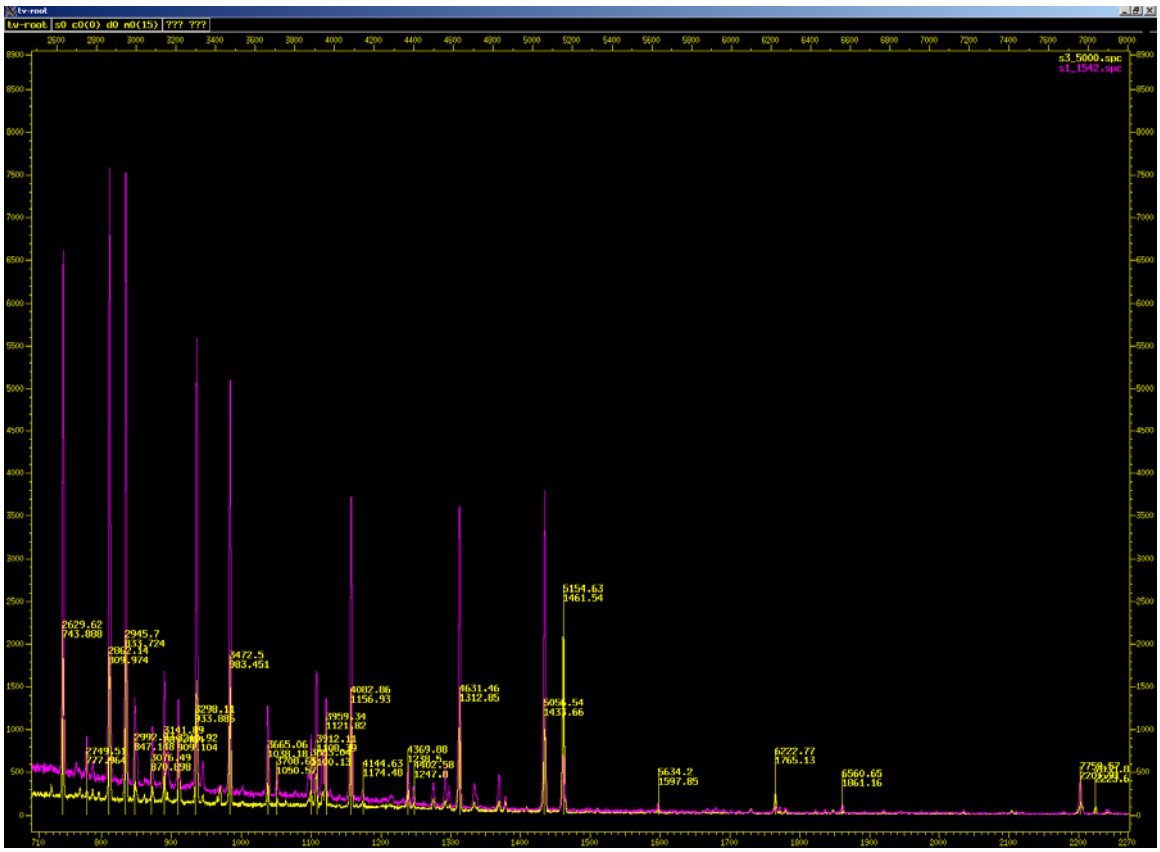

Figure 16: Higher energy (~700-2270 keV) photon energy spectra from Sample 1 (low-dose run) and Sample 3 (high dose run) are compared. At each peak marker, displayed by the vertical lines, the upper number is the peak centroid in units of channels and the lower number is the photon energy in units of keV as calculated using the centroid value.

The total activity from unidentified photons was added to the activities of the identified nuclides, assuming branching ratios of unity. Several nuclides could not be identified yet were predicted to be present by PHITS simulations and DCHAIN SP 2001 [23, 24] analysis. The calculated activities were added to the measured activities. The isotopes and activities shown in Table 1 formed the basis for comparisons to limits on activities for transportation purposes. A significant portion of the activity came from the copper spacers and sample holders.

Table 1: Activities measured and predicted in the irradiated target assemblies.

Low-Dose Run			High-Dose Run		
Identification	Isotope	Activity Bq	Identification	Isotope	Activity Bq
Identified by photons	44Sc	2.92E+02	Identified by photons	44Sc	3.73E+03
	46Sc	1.24E+03		46Sc	1.24E+03
	47Sc	3.63E+02		47Sc	5.38E+03
	48Sc	4.58E+03		48Sc	4.58E+03
	48V	4.06E+01		48V	4.87E+03
	51Cr	5.87E+02		51Cr	7.49E+03
	52Mn	4.06E+01		52Mn	5.59E+03
	56Co	4.06E+01		56Co	8.78E+02
	57Co	4.06E+01		57Co	2.02E+03
	58Co	4.27E+02		58Co	6.33E+03
	67Ga	1.73E+03		67Ga	2.19E+04
	69Ge	3.59E+02		69Ge	4.57E+03
	71As	5.81E+02		71As	8.17E+03
	72Ga	2.01E+02		72Ga	4.43E+03
	72Zn	1.64E+02		72Zn	2.56E+03
	74As	6.43E+02		74As	7.80E+03
	76As	8.73E+01		76As	1.68E+03
	77Br	1.24E+04		77Br	1.63E+03
	77Ge	9.65E+01		77Ge	9.57E+02
	7Be	2.08E+03		7Be	9.01E+03
	87Y	1.22E+02		87Y	1.23E+03
	24Na	3.88E+01		24Na	4.97E+02
	43K	1.78E+01		43K	4.45E+02
	47Ca	2.00E+01		47Ca	2.97E+02
Predicted Activities, non-gamma emitters	Ge 71	2.22E+04	Predicted Activities, non-gamma emitters	Ge 71	2.22E+04
	Cu 66	1.69E+04		Cu 66	1.69E+04
Predicted Activities, could not identify	Ni 66	1.69E+04	Predicted Activities, could not identify	Ni 66	1.69E+04
	Sr 87m	6.98E+03		Sr 87m	6.98E+03
	Kr 79	6.61E+03		Kr 79	6.61E+03
	P 32	5.85E+03		P 32	5.85E+03
	Y 89m	4.68E+03		Y 89m	4.68E+03
	P 33	3.77E+03		P 33	3.77E+03
	H 3	3.45E+03		H 3	3.45E+03
	Fe 59	3.26E+03		Fe 59	3.26E+03
	Unknowns	3.05E+03		Unknowns	8.29E+03
	Sum	1.20E+05		Sum	2.06E+05

Post-Irradiation Examination

Relatively low activation doses of the specimens allowed us to use the LAMDA facility at ORNL for material analysis. The facility was designed for work with low activity samples with activation dose rates below 60 mrem/hr at 30 cm. We started the material analysis with the stack of foils that was irradiated for a longer period of time. The analysis showed very low damage level in that stack. The second stack that was irradiated for a shorter period was not analyzed at all because we did not expect to see any damage there.

Electrical Resistivity

A four probe technique was used to measure electrical resistivity. This technique involves the passage of a current through outer electrical contacts of the sample, with resistivity measured as a function of the voltage measured across two inner contact points of known separation in accordance with ASTM standard B193-02 [25]. Images illustrating the design of the electrical resistivity holder are shown in Figure 17 and Figure 18. The holder consists of two current leads which are in electrical contact with the sample through selectively insulated support threads that hold the assembly together and press the current pads against the sample. A Keithley Model 238 Source Measure Unit was used to supply the 1.0 A current through the outer contacts at the ends of the sample and a Keithley Model 183 Sensitive Digital Voltmeter was used to measure the voltage drop taken at specified locations along the samples. The inner voltage contacts consist of sheathed pogo-type pins spaced 2.54 mm apart. By careful positioning the sample in the holder, the voltage pins could be placed either inside the irradiated region of the sample or further away to measure the annealed condition of the sample. The accuracy of both the potential measurement and the current sourcing is rated as <0.1%. The direction of electrical current passing through the sample was switched following each voltage measurement to cancel out effects of thermally driven EMF.

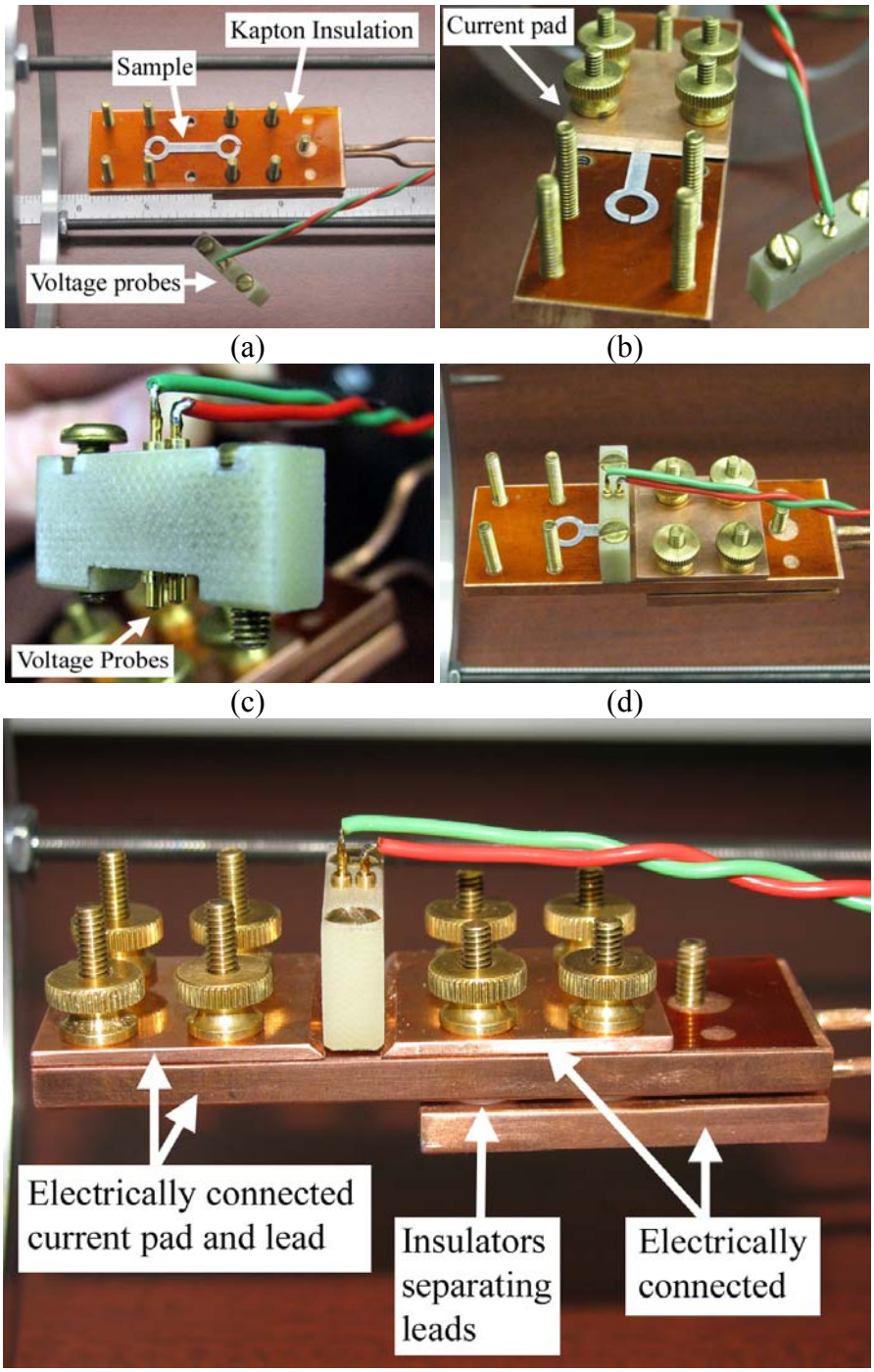

Figure 17: Images showing the loading of a sample in the holder designed for electrical resistivity testing. (a) Sample placed on Kapton insulator at desired location, (b) current pad placed on one end of sample, (c) close-up view of pogo-type pin voltage probes mounted in epoxy support structure, (d) top-view of voltage pin support structure in place with voltage probes contacting the sample in the irradiated region, and (e) assempled holder consisting of the current leads contacting the sample through the current pads. Insulators are separating the two leads.

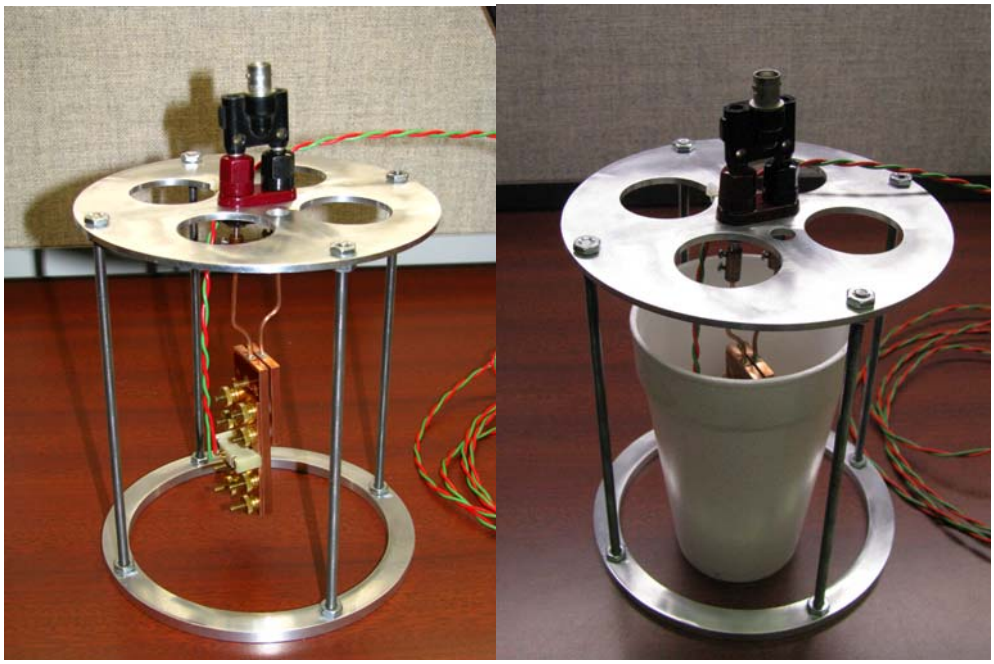

Figure 18: Electrical resistivity holder and support frame. Holder can be lowered into a styrofoam cup for liquid nitrogen emersion.

Testing was performed on both the ion irradiated section of the sample as well as in the annealed locations away from the ion damage. Tests were conducted with the four probe holder submerged in liquid nitrogen. Care was taken in the design to minimize thermal losses associated through the connections and wiring of the system. The resistivity holder took approximately two minutes after submersion to reach equilibrium with the boiling liquid nitrogen. Testing of the system showed that subsequent exposure of the resistivity holder for times up to 15 minutes following submersion and attainment of the cryogenic temperatures resulted in no significant changes in measured voltage and thus resistivity. To ensure that small daily variations in the boiling temperature of the nitrogen resulting from atmospheric changes were taken into account, a correction factor was used to correlate the measured data to a 77 K reference temperature. The resistivity at 77 K is calculated from the following equation:

$$\rho_{77K}\,(n\Omega - m) = \frac{(V \times A)}{(I \times L)} \frac{1}{(1 + \alpha(T_R - 77))}$$

where

V = measured voltage (nV)
A = cross-section area of gage section (m^2)
I = applied current (1.0 A)
L = distance between inner electrodes (0.00254 m)
α = temperature coefficient of electrical resistivity (0.0043 K^{-1})
T_R = temperature recorded during measurement (K)

Microhardness Measurements

To determine the best parameters for microhardness measurements taken on the aluminum samples, testing was performed on a non-irradiated control specimen that had been annealed under the same conditions as the samples later irradiated. Five measurements were made at 5, 10, 25, 50, 100, 200 and 300 g loads and dwell time of 15 seconds using a Buehler Micromet 3 hardness indenter equipped with a Vickers tip.

A plot of this data is shown in Figure 19. From the test measurements it was apparent that surface features such as oxide film and surface irregularities were affecting the measured hardness values at loads below 50 g along with increasing the range in measured data. Similar reports of surface hardening at loads near 50 g and softening at loads less than 15g in annealed copper have previously been reported [26], though the causes are unknown. The hardness values appear to plateau to consistent values at loads between 100 and 200 g, and are within the 15 to 20 kg/mm^2 value reported throughout literature for annealed aluminum. Indents made under 300 g loads were too large to measure using the optics of the instrument. Also plotted in Figure 19 is the indenter penetration depth versus load. Assuming that the plastic zone around the indent is between 7 to 10 times that of indenter penetration depth, at loads above 100 g the plastic zone will be approaching the thickness of the aluminum samples (approximately 240 μm). Therefore, further testing on the irradiated samples was performed at 100 g loads.

Measurements of the irradiated material were performed using a Mitutoya model Vickers indenter (100 g load, 15 second dwell time) located within the LAMDA laboratory due to the residual activity of the samples. Prior to testing of the irradiated samples, measurements were performed on four annealed samples. The annealed material showed some sample to sample variation, though the 16.4 kg/mm^2 average measured hardness readings of the Mitutoya instrument was comparable to the 18.8 kg/mm^2 average measured from the Buehler instrument as well as the range of published data for annealed aluminum. Hardness measurements were conducted on the beam damaged regions of samples 1, 8, 15, 16 and 24 from the higher dose sample stack. For comparison, measurements were also made on one as-machined sample which would exhibit some level of cold work.

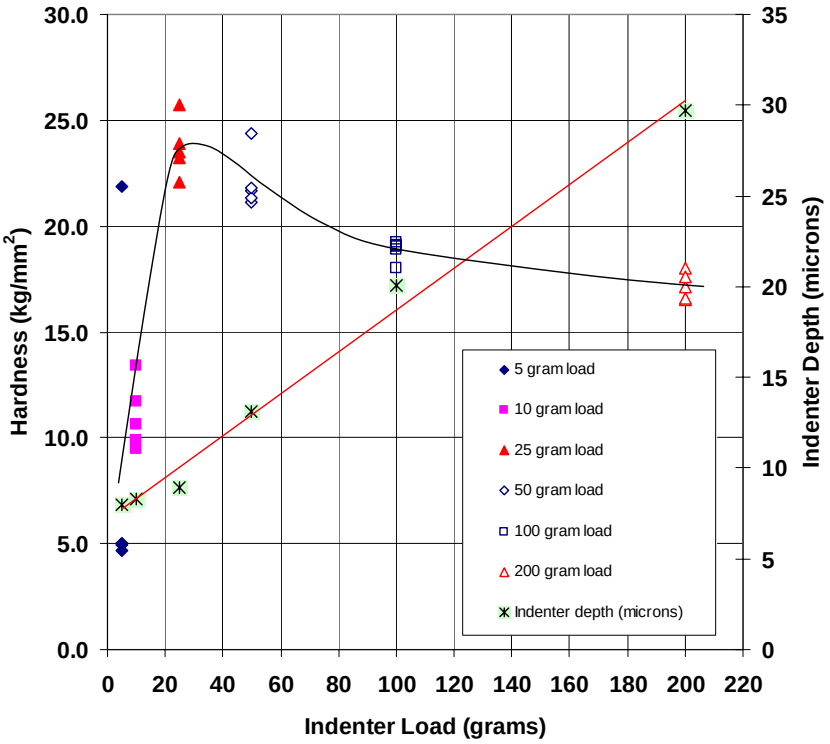

Figure 19: Measured hardness and indenter penetration depth for an non-irradiated control specimen versus indenter load.

Transmission Electron Microscopy

Samples for transmission electron microscopy (TEM) were cut from the irradiated regions of sample numbers 2, 4, 6, 8, 14, 17 and 22 along with one sample from an as-annealed sample. Samples were jet-polished with an electrolyte of 10 vol.% H_2SO_4 in methanol. Samples were examined in both a Philips/FEI Tecnai T20 and CM200-FEG microscopes.

Results

Electrical Resistivity

Tests were conducted on an annealed sample, number 6 taken from the unirradiated sample stack, to gauge the measure of sample repeatability. Following the first measurement run of the sample, the resistivity holder was allowed to warm to room temperature and then submersed again into the liquid nitrogen bath without undergoing any adjustment to the sample position. After the second measurement, the sample was warmed to room temperature, removed from the holder, flipped over, and then reset into the sample holder for a final test measurement at cryogenic temperatures. The results are shown below in Table 2. The measured voltage readings are shown to vary between a high and low range of values, which are associated with the measured readings corresponding to the switch in current direction. The resistivity of the sample is calculated from the averaged value of the measured voltage readings. Repeatability was determined to be sufficient with changes in resistivity < 1%.

Table 2: Sample repeatability testing performed on an annealed specimen.

Sample #	Run #	Test Date	Barometric Pressure (inches Hg)	Average Thickness (mm)	Average Width (mm)	Measure Voltage Readings (nano-volt)					Temp. Liq. N_2 (K)	Resistivity (nΩ-m), at 77 K
6	run 1	1-Apr-08	30.09	0.24	2.95	7980	7975	7983	7974	7992	77.050	2.2231
						7962	7975	7984	7973	7975		
6	run 2	1-Apr-08	30.09	0.24	2.95	7978	7982	7970	7983	7967	77.050	2.2223
						7980	7976	7972	7962	7972		
6	run 3	1-Apr-08	30.09	0.24	2.95	8022	7968	8023	7972	8019	77.050	2.2285
						7971	8023	7969	8026	7973		

% Change between run #1 and #2 =	-0.04
% Change between run #1 and #3 =	0.24
% Change between run #2 and #3 =	0.28

The 10 μm accuracy in dimensional measurement of the sample width and thickness by using a digital micrometer was found to be insufficient, due to the significant scatter in the initial testing of the irradiated and annealed samples. A more precise determination of sample dimensions was sought through the imaging of the width and thickness profiles of the individual samples by optical microscope at the locations where the voltage probes were placed. Images of the sample widths were taken at magnifications of 25x and sample thicknesses at 40x. Samples were placed on a glass slide for width measurements, or sandwiched between glass slides and lightly gripped in a vice to provide a profile view of the sample thickness. Care was taken to limit the error associated with tilting the sample under observation. The gripped samples were allowed to protrude from the edge of the glass slides to ensure an unobstructed view of the sample profile. Calibration measurements were made using a scale on a metal ruler at 25x and 40x magnification.

Image analysis from each location where resistivity measurements were taken, consisted of the placement of a line representing the estimated boundary edge of the sample that best averages the local surface roughness. The distance between the averaged surface boundaries was measured through image analysis software and converted through the determined magnification calibration into the actual value of thickness or width. An

example of the thickness and width images for the annealed section of sample number 16 is shown below in Figure 20.

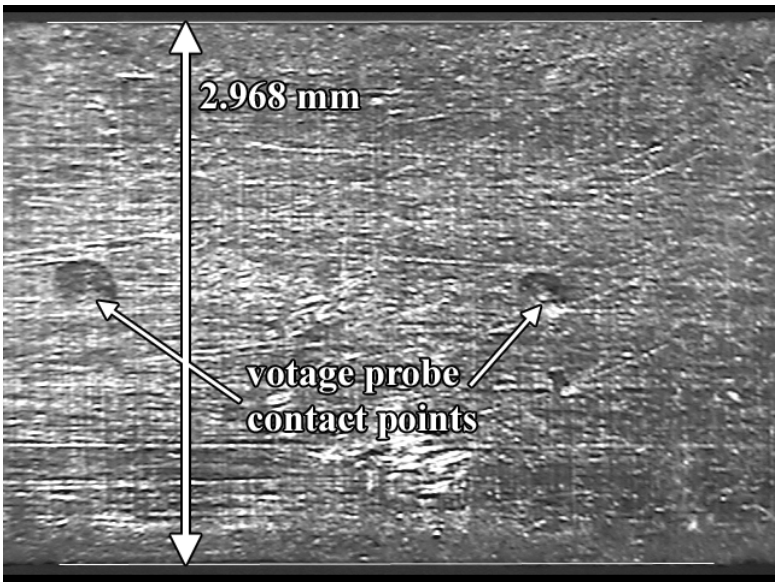

(a)

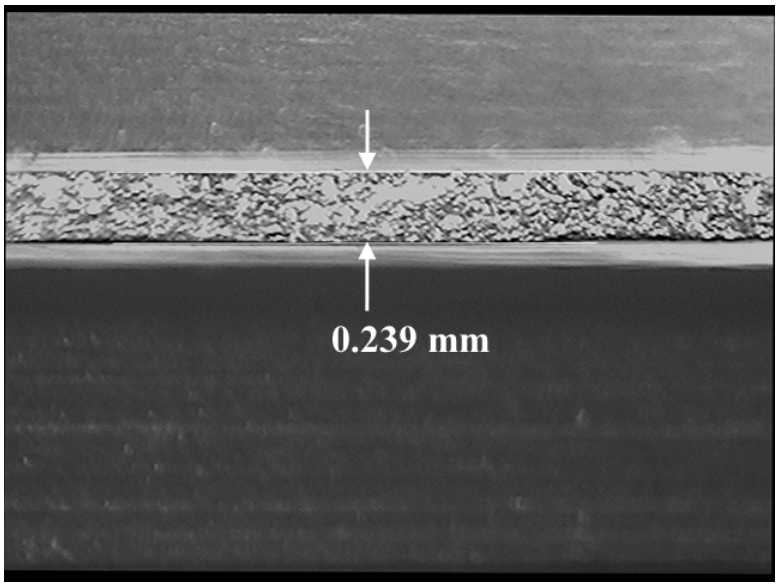

(b)

Figure 20: Optical images of the (a) sample width and (b) thickness taken of annealed sample number 16 at the location of the voltage probe contacts.

The average thickness and width of the eleven measured samples was 0.241±0.011 mm and 2.974±0.052 mm, respectively. It is estimated that the error associated with image analysis, which incorporates both the error of interpretation regarding the positions of the sample edges and calibration errors of the scaling factor, was approximately ±5.2 μm.

Using the optical microscope for accurate measurements of sample thickness and width, the electrical resistivity was calculated for the measured voltage readings of the eleven irradiated test samples (#'s 2, 4, 8, 10, 12, 16, 17, 18, 20, 22 and 26). The resistivity of the samples was also determined for the annealed region away from the beam spot but within the uniform gauge section of the samples. The measured data for the samples and their calculated resistivity are shown in Table 3.

Table 3: Results of electrical resistivity measurements.

Resistivity Measurements

Sample Stack #2, 0.01 dpa
Testing under liquid nitrogen

Constants:

L(m) =	0.00254	spaceing between voltage probes
I (amp) =	1	measurement current
α (K^{-1}) =	0.0043	temperature coefficient

Sample #	Location Irrad. (center)	Location Annealed (end)	Test Date	Barometric Pressure (inches Hg)	Measured Thickness (mm)	Measured Width (mm)	Measure Voltage Readings (nano-volt) #1	#2	#3	#4	#5	Temp. Liq. N_2 (K)	Resistivity (nΩ-m), at 77 K
	X		4-Apr-08	29.97	0.23842	2.9753	8016	8012	8010	8011	8014	77.014	2.2378
							8013	8013	8018	8009	8015		
							8014	8012	8015	8016	8017		
							8013	8007	8012	8011	8013		
							8016	8012					
2		X	4-Apr-08	29.97	0.23842	2.9753	7999	7988	7997	7984	7997	77.014	2.2326
							7991	7998	7984	7999	7993		
							7994	7999	7986	8002	7986		
							8005	7999	8006	7993	8000		
							7984	8000					
												difference =	0.0051
	X		2-Apr-08	30.36	0.250499	2.96783	7972	7970	7968	7978	7964	77.129	2.3310
							7976	7965	7976	7961	7973		
							7962	7958	7975	7960	7960		
							7972	7963	7978	7972	7965		
4		X	2-Apr-08	30.36	0.24899	2.95784	7880	7867	7874	7867	7874	77.129	2.2813
							7870	7874	7880	7865	7875		
							7866	7872	7868	7879	7875		
												difference =	0.0497
	X		4-Apr-08	29.92	0.24899	2.9678	7877	7862	7873	7860	7869	77.000	2.2883
							7864	7869	7855	7867	7859		
							7868	7873	7860	7878	7856		
							7856	7854	7875	7859	7878		
							7857	7870					
8		X	4-Apr-08	29.92	0.24295	2.9703	7764	7759	7770	7761	7766	77.000	2.2054
							7769	7759	7764	7758	7766		
							7768	7759	7766	7751	7774		
							7750	7764	7756	7772	7750		
							7769						
												difference =	0.0828

Sample #	Location		Test Date	Barometric Pressure	Measured Thickness	Measured Width	Measure Voltage Readings (nano-volt)					Temp. Liq. N_2 (K)	Resistivity (nΩ-m), at 77 K
	Irrad. (center)	Annealed (end)		(inches Hg)	(mm)	(mm)	#1	#2	#3	#4	#5		
	X		4-Apr-08	29.95	0.23994	2.99778	7931	7933	7926	7923	7921	77.009	2.2448
							7924	7923	7926	7928	7928		
							7927	7932	7926	7926	7927		
							7932	7924	7929	7924	7934		
							7929	7930					
10		X	4-Apr-08	29.95	0.24144	3.0252	7890	7887	7893	7884	7890	77.009	2.2685
							7887	7890	7893	7888	7890		
							7891	7888	7884	7888	7889		
							7887	7897	7893	7890	7884		
							7888	7892					
												difference =	-0.0237
	X		2-Apr-08	30.35	0.22937	3.01275	8108	8083	8109	8094	8119	77.126	2.2028
							8096	8115	8095	8105	8096		
							8102	8096	8108	8098	8102		
							8098	8095					
12		X	2-Apr-08	30.35	0.23389	3.010259	7918	7933	7903	7934	7903	77.126	2.1937
							7924	7926	7906	7927	7915		
							7928	7905	7932	7925	7903		
							7928	7902					
												difference =	0.0091
	X		3-Apr-08	30.1	0.236917	2.97032	8094	8066	8092	8068	8091	77.053	2.2380
							8068	8091	8068	8089	8070		
							8090	8066	8095	8085	8069		
							8086	8069	8092	8069	8086		
							8066						
16		X	3-Apr-08	30.1	0.23999	2.96782	8057	8068	8048	8068	8048	77.053	2.2598
							8071	8048	8080	8042	8077		
							8045	8078	8048	8073	8048		
							8070						
												difference =	-0.0218
	X		1-Apr-08	30.09	0.24144	2.9903	7876	7863	7859	7853	7844	77.050	2.2337
							7843	7857	7844	7865	7854		
							7865	7854	7872	7862	7860		
							7866	7867	7864	7860	7861		
							7863	7864	7863	7864	7862		
17		X	1-Apr-08	30.09	0.24597	2.9753	7925	7907	7910	7914	7903	77.050	2.2801
							7915	7902	7925	7914	7920		
							7911	7916	7913	7917	7922		
							7912	7922	7922	7921	7915		
												difference =	-0.0464

Sample #	Location Irrad. (center)	Location Annealed (end)	Test Date	Barometric Pressure (inches Hg)	Measured Thickness (mm)	Measured Width (mm)	Measure Voltage Readings (nano-volt) #1	#2	#3	#4	#5	Temp. Liq. N_2 (K)	Resistivity (nΩ-m), at 77 K
	X		3-Apr-08	30.1	0.2413	2.959	8014	8010	8024	8000	8022	77.053	2.2523
							8004	8023	8006	8021	8007		
							8022	8000	8024	8005	8022		
							8006	8025	8008	8022	8005		
							8025	8004	8024	8006	8028		
18		X	3-Apr-08	30.1	0.2413	2.959	7935	7945	7933	7945	7931	77.053	2.2311
							7947	7930	7945	7940	7935		
							7937	7936	7937	7940	7934		
							7943	7940	7941	7939	7940		
												difference =	0.0213
	X		3-Apr-08	30.19	0.23843	2.97032	8187	8165	8196	8155	8198	77.079	2.2791
							8155	8198	8155	8182	8165		
							8183	8176	8182	8183	8169		
							8182	8175	8180	8170	8183		
							8170						
20		X	3-Apr-08	30.19	0.23843	2.97781	8177	8103	8158	8182	8165	77.079	2.2828
							8182	8180	8162	8178	8168		
							8175	8162	8180	8162	8181		
							8165	8180	8175	8178	8176		
												difference =	-0.0037
	X		3-Apr-08	30.1	0.24144	2.9337	8017	8018	8016	8014	8019	77.053	2.2351
							8018	8018	8017	8016	8028		
							8008	8028	8004	8028	8004		
							8034	8000	8020	8013	8019		
							8013	8027	8008	8021	8014		
22		X	3-Apr-08	30.1	0.24597	2.921	7868	7838	7866	7845	7852	77.053	2.2209
							7855	7854	7857	7845	7858		
							7843	7858	7858	7846	7854		
							7848	7852	7858				
												difference =	0.0143
	X		4-Apr-08	29.94	0.23842	2.9528	7997	7986	7997	7986	7999	77.006	2.2153
							7987	7993	7993	7992	7997		
							7998	7998	7985	7993	7985		
							7998	7989	7997	7985	7997		
							7992	7997					
26		X	4-Apr-08	29.94	0.23842	2.9854	7874	7873	7872	7874	7873	77.006	2.2067
							7877	7873	7879	7876	7874		
							7877	7880	7871	7871	7876		
							7873	7877	7878	7874	7873		
							7876	7873	7876				
												difference =	0.0086

The resistivity data from Table 3 is plotted in Figure 21, while the change in resistivity between the irradiated and annealed values from each tested sample is plotted in Figure 22. In addition, a summary of the data from Table 3 is as follows:

Sample Dimension Statistics

	t (nm)	w (nm)
average =	0.2410	2.9738
maximum =	0.2505	3.0252
minimum =	0.2294	2.9210
Range =	0.0211	0.1042
Deviation =	0.0106	0.0521

Measured Voltage Changes

average measured voltage (nV) =	7965.8
Max (nV)=	8198.0
Min (nV) =	7750.0
Range (nV) =	448.0

Resistivity Changes

	ρ (nΩ-m)
average resistivity (all samples) =	2.2464
Max (all samples) =	2.3310
Min (all samples) =	2.1937
Range (all samples) =	0.1373
Deviation (all samples) =	0.0686
average resistivity (irradiated) =	2.2507
max (irrad) =	2.3310
min (irrad) =	2.2028
Range in irradiated values =	0.0803
average resistivity (annealed) =	2.2421
max (annealed) =	2.2828
min (annealed) =	2.2828
Range in annealed values =	0.0407

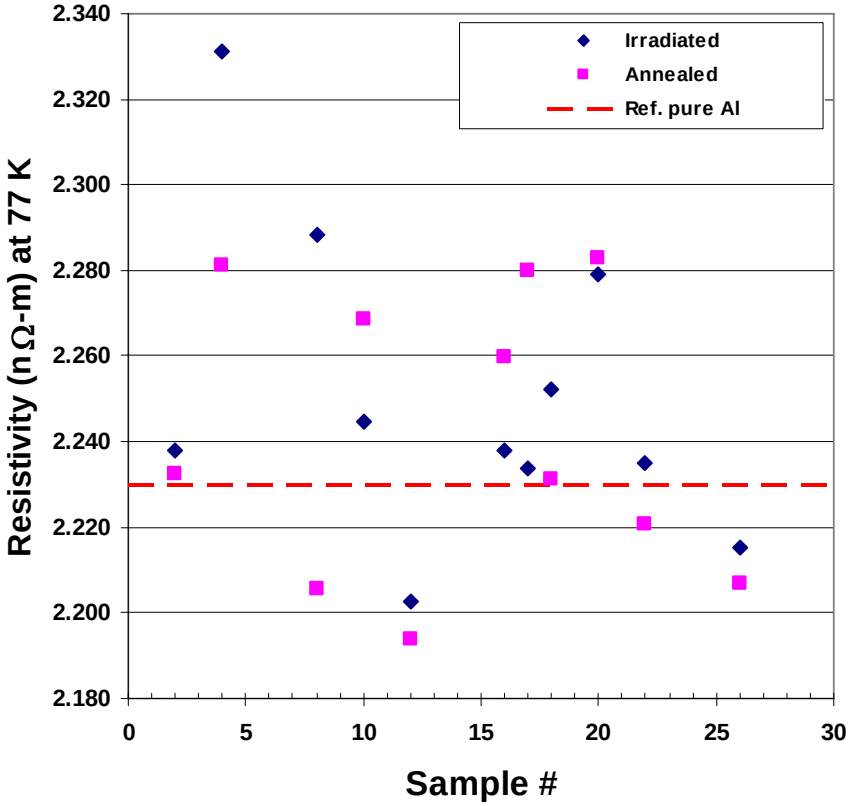

Figure 21: Electrical resistivity data measured from eleven test samples showing taken from the irradiated and annealed regions of the samples.

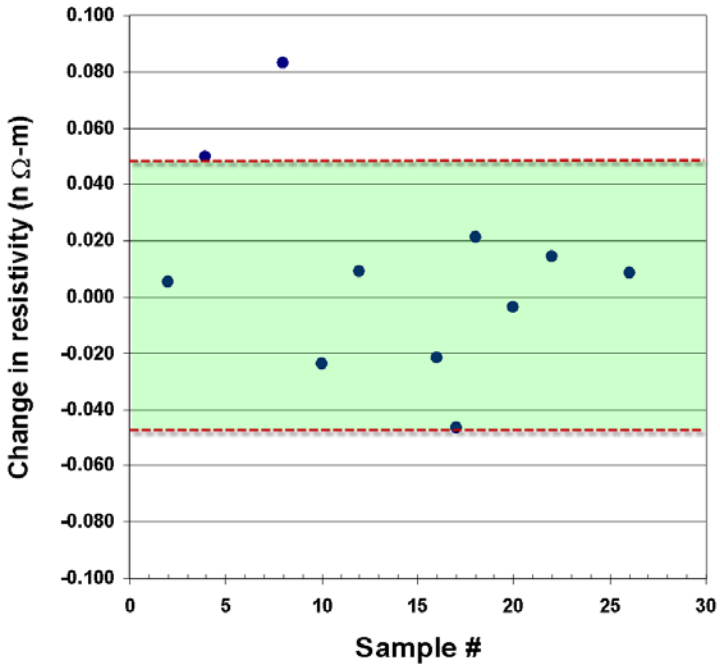

Figure 22: The change in resistivity between the irradiated and annealed sections of the eleven samples tested. The region within the dashed lines is the error associated with making a ±5.2 µm variation in measured thickness.

It is apparent from the above figures that no clear trend related to the changes in resistivity versus sample position, and thus dose, can be obtained. The resistivity for all measurements is within 4.5% of a reported value for pure aluminum of similar impurity level. It should be noted that less pure grades of aluminum are expected to have a resistivity of approximately 2.3 nΩ-m at 77 K. While no specific data on electrical resistivity changes in irradiated aluminum were found in literature, there is a substantial database for copper and copper alloys examined for the Department of Energy's Fusion Energy Program. Experimental evidence has shown that an approximate resistivity increase of 0.5 nΩ-m per dpa occurs in copper [27] and that resistivity increases associated with defect clusters saturate around 1.2 nΩ-m [28] with further increases attributed to transmutation products. If a similar increase in electrical resistivity is assumed for aluminum, the 0.01 dpa irradiation would likely not show an increase over the measurement error.

The measured resistivity of the aluminum samples is dependent on the sample dimensions, whose tolerances are limited by machining techniques. These tolerances were found to vary ±0.011 mm in thickness and ±0.0052 mm in width. This translates to variations of 4.56% in thickness and 1.75% in width. These dimensional tolerances were within the resolution of the digital micrometer. Analysis of the sample dimensions by optical microscopy improved the measurement error to ±5.2 μm, for both thickness and width. A change in sample thickness of ±5.2 μm, assuming all other variables to remain constant, would result in a ±0.048 nΩ-m change in resistivity. This error band is represented in Figure 22, and is shown to dominate over the measured data.

Microhardness

Microhardness measurements were performed on annealed samples 2, 3, 4 and 5 from the test stack and samples 1, 8, 16 and 24 from the higher dose irradiated sample stack. In addition, measurements were also made on an as-machined sample that had not been annealed. The results of the hardness measurements are plotted in Figure 23. The measured hardness of the irradiated samples was within 4% of the average value of the annealed material. The range in measured hardness of the irradiated samples was much greater than that of the annealed material. No specific trend in hardness data was observed for the samples as a function of penetration depth of the ion beam.

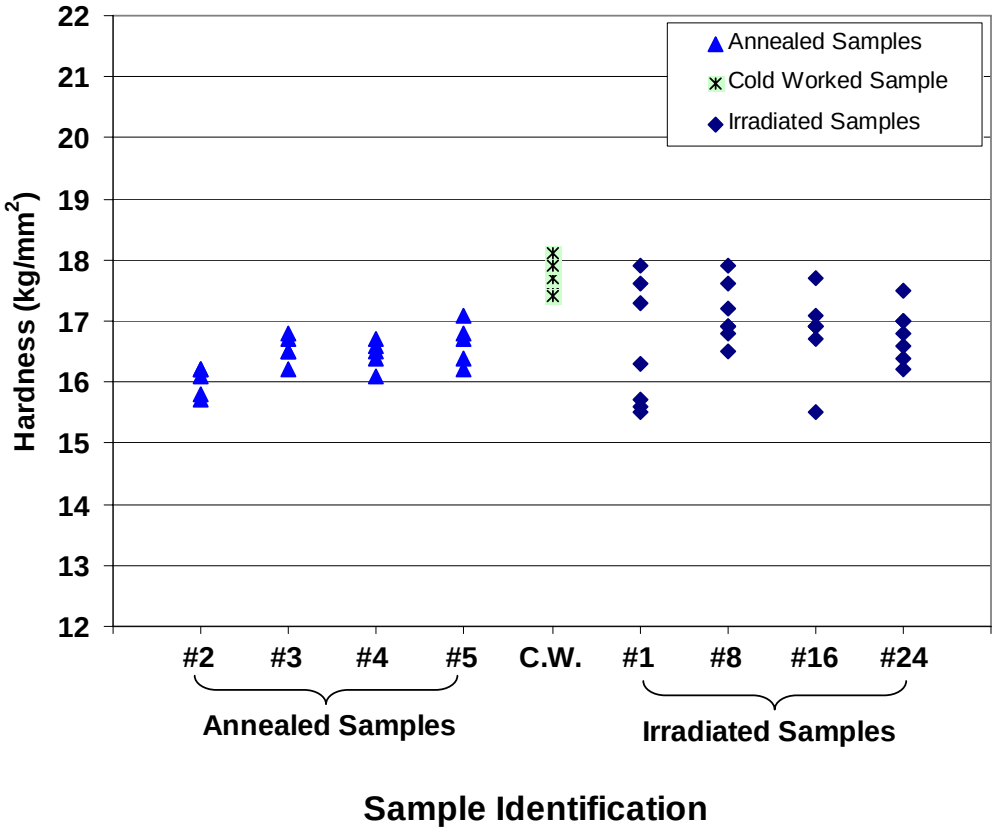

Figure 23: Vickers hardness of annealed, cold worked (c.w.) and irradiated samples.

The hardness values for the cold worked sample were not significantly higher than that of the as-annealed condition and were within range of reported literature values for annealed aluminum. This suggests that either that the samples showed a low level of cold rolling during fabrication of the aluminum sheet from which the irradiation samples were cut from, or that annealing of defects can occur at ambient temperatures. If a low level of cold work was used by the manufacturer of the aluminum sheet in order to achieve the dimensional tolerances required for the product, very little stored energy would be available during the annealing treatment of the samples to eliminate defects in the microstructure.

Transmission Electron Microscopy

Microstructural analysis of irradiation defects was conducted through transmission electron microscopy (TEM) of irradiated samples 2, 4, 6, 8, 14, 17 and 22 as well as one of the as-annealed specimens. The as-annealed material consisted of large equiaxed grains of 30 to 40 microns in size, some of which contained subgrain formations (Figure 24). In addition, dislocation network tangles were also visible within the microstructure, though most of the grains and subgrain formations were devoid of defects. These defects are consistent with material that has not been completely recrystallized through

annealing, resulting in sample to sample variation in both electrical resistivity and hardness. Short length dislocation segments that are typically observed in roughly handled specimens were not observed in the material.

The irradiated materials selected for examination allowed for a representative sampling of the electronic and nuclear stopping regimes expected in the sample stack. Representative TEM images from these samples are shown in Figure 25. Sample number 2 revealed the highest amount of defect damage observed in all the samples. Dislocation loops, clearly observable in Figure 25 (a), were inhomogeneous in appearance within the grains of the sample with a dislocation loop density of approximately 8 x 10^{19} m^{-3}. Samples 4, 6 and 8 were similar in the density of loops and appear to be slightly lower in concentration than that of samples 14 and 17, where the peak of nuclear stopping is occurring. However, dislocation loop densities were very low within these samples and are at best estimated to be less than 1 x 10^{18} m^{-3}. Sample number 22 was beyond the stopping range of the beam and correspondingly showed no radiation damage.

The high concentration of dislocation loops observed in sample 2, indicates that the high energy ion beam did have a considerable effect in generating displacement damage through electronic stopping. While displacement damage was observed through the development of dislocation loops in all the irradiation samples examined, with the exception of #22, the network of dislocation lines, tangles, and subgrain boundaries dominate the microstructure. Therefore, the level of defect damage generated during irradiation was not enough to show up over the statistical averaged values of electrical resistivity and hardness of the as-annealed samples.

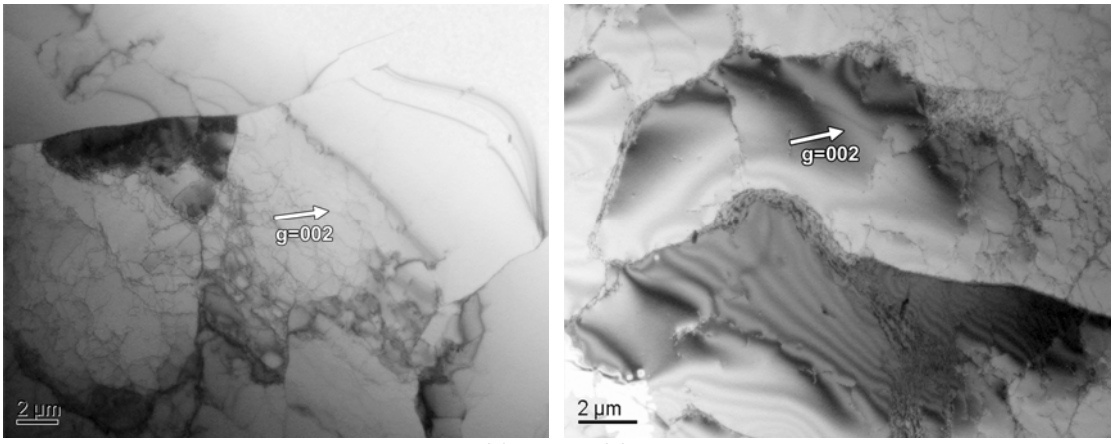

(a) **(b)**

Figure 24: (a) Micrographs of as-annealed material showing dislocation networks along with (b) subgrain structures in the material.

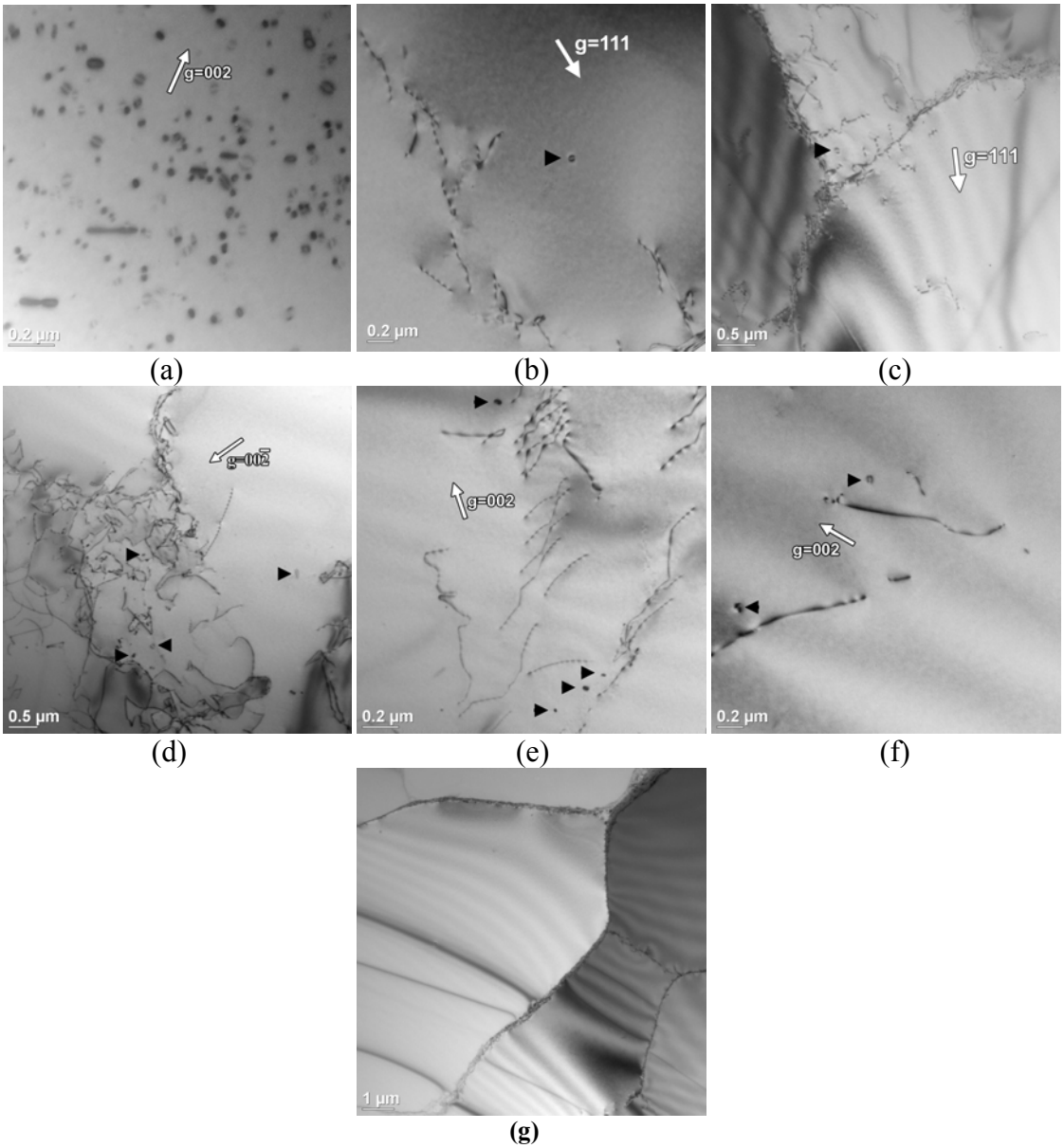

Figure 25: Micrographs of irradiated samples #'s (a) 2, (b) 4, (c) 6, (d) 8, (e) 14, (f) 17, and (g) 20. Black arrows help to indicate locations of radiation induced dislocation loops. Sample #20 was beyond the stopping depth of the ion beam and revealed no radiation induced defects.

Conclusions

An intense beam of 122 MeV/u (9.3 GeV) ^{76}Ge ions was stopped in aluminum samples at the Coupled Cyclotron Facility at NSCL, MSU. Attempts were made at ORNL to measure changes in material properties by measuring changes in electrical resistivity and microhardness, and by inspecting transmission electron microscopy (TEM) data for defect density caused by radiation damage, as a function of depth and integrated ion flux. These measurements are relevant for estimating damage to components at a rare isotope beam facility. No changes in electrical resistivity and in microhardness above experimental uncertainties were measured. The significant concentration of dislocation loops observed by TEM in a sample taken from the 0.48 mm depth of the highest dose sample stack indicates that the high energy ion beam did have a considerable effect in generating displacement damage through electronic stopping. While displacement damage was observed through the development of dislocation loops in all the irradiation samples examined, the network of dislocation lines, tangles, and subgrain boundaries dominate the microstructure. Therefore, the level of defect damage generated during irradiation was not enough to show up over the statistical averaged values of electrical resistivity and hardness of the as-annealed samples.

Bibliography and References Cited

1. U.S. Department of Energy Press Release, December 11, 2008; http://www.energy.gov/news/6794.htm
2. L. K. Mansur, "Materials Issues in High Power Accelerators", Nucl. Instr. Meth., A562 (2006) 666–675
3. W. Stein, L.E. Ahle, S. Reyes, "Beam Dump Design for Rare Isotope Accelerator Fragmentation Line", UCRL-TR221121. Lawrence Livermore National Laboratory, (May 5, 2006).
4. Hiroshi Iwase, Tadahiro Kurosawa, Takashi Nakamura, Nobuaki Yoshizawa, and Jun Funabiki, "Development of Heavy Ion Transport Monte Carlo Code", Nucl. Inst. Meth. B183, 374(2001).
5. N.V. Mokhov, "The Mars Code System User's Guide", Fermilab-FN-628 (1995).
6. N.V. Mokhov, K.K. Gudima, C.C. James, M.A. Kostin, S.G. Mashnik, E. Ng, J.F. Ostiguy, I.L. Rakhno, A.J. Sierk, S.I. Striganov, "Recent Enhancements to the MARS15 Code", Radiation Protection and Dosimetry, vol. 116, part 2, pp. 99-103 (2005); Fermilab-Conf-04/053 (2004).
7. N.V. Mokhov, K.K. Gudima, S.G. Mashnik, I.L. Rakhno, A.J. Sierk, S.I. Striganov, "Physics Models in the MARS15 Code for Accelerator and Space Applications", in Proc. of International Conference on Nuclear Data for Science and Technology, Santa Fe, NM, 2004, AIP Conf. Proc. 769, part 2, pp. 1618-1623; Fermilab-Conf-04/269-AD (2004).
8. MARS code system at Fermi National Accelerator Laboratory, Accelerator Division; http://www-ap.fnal.gov/MARS/
9. H.G.Hughes et al., "MCNPX for Neutron-Proton Transport", International Conference on Mathematics and Computation, Reactor Physics and Environmental Analysis in Nuclear Applications, American Nuclear Society, Madrid, Spain, September 27-30, 1999.
10. J. F. Ziegler, J. P. Biersack and U. Littmark, "The Stopping and Range of Ions in Solids", Pergamon Press, New York, 1985; http://www.SRIM.org/
11. G. Battistoni, S. Muraro, P.R. Sala, F. Cerutti, A. Ferrari, S. Roesler, A. Fasso`, J. Ranft, "The FLUKA Code: Description and Benchmarking", Proceedings of the Hadronic Shower Simulation Workshop 2006, Fermilab 6--8 September 2006, M. Albrow, R. Raja eds., AIP Conference Proceeding 896, 31-49, (2007)
12. A. Fasso`, A. Ferrari, J. Ranft, and P.R. Sala, "FLUKA: a Multi-Particle Transport Code", CERN-2005-10 (2005), INFN/TC_05/11, SLAC-R-773; http://www.fluka.org/
13. A. Dunlop, et al., "Effects Induced by High Electronic Excitations in Pure Metals: a Detailed Study in Iron", Nucl. Instr. and Meth., B90 (1994) 330-338
14. A. Iwase and T. Iwata, "Effect of Electron Excitation on Radiation Damage in FCC Metals", Nucl. Instr. and Meth., B90 (1994) 322-329
15. A. M. Rutherford and D. M. Duffy, "Modelling Swift Heavy Ion Irradiation in Iron", Nucl. Instr. and Meth., B267 (2009) 53-57
16. B.D.Wirth, private communication

17. The Final Report to DOE on Development of a Concept for High Power Beam Dumps and Catchers, and the Pre-separator Area Layout for Fragment Separators for RIA (DE-FG02-04ER41313); submitted on November 21, 2007.
18. Goodfellow Corporation, 305 High Tech Drive, Oakdale, PA 15071-3911, USA; http://www.Goodfellow.com
19. K. Farrell and J.T. Houston, "Suppression of Radiation Damage Microstructure in Aluminum by Trace Impurities", J. Nucl. Mater., 83 (1979) 57-66.
20. Handbook of Aluminum, vol. 2, eds. G.E. Totten and D.S. MacKenzie, CRC Press, Boca Raton, FL, 2003, pgs. 203-215.
21. R. Ladbury et. al., "Performance of the High-Energy Single-Event Effects Test Facility (SEETF) at Michigan State University's National Superconducting Cyclotron Laboratory (NSCL)", IEEE Transactions on Nuclear Science, Vol. 51, No. 6, December 2004, pp. 3664-3668.
22. T. Baumann, T. Ginter, private communications
23. H. Takada and K. Kosako, "A Code System for Analyzing Decay and Build-up Characteristics of Spallation Products," JAERI-Data/Code-99-008, March 1999.
24. T. Kai, F. Maekawa, et al., "DCHAIN-SP2001: High Energy Particle Induced Radioactivity Calculation Code," JAERI-Data/Code 2001-016 (In Japanese) (2001).
25. "Standard Test Method for Resistivity of Electrical Conductor Materials", ASTM Designation B 193-87. ASTM Standards Online, American Society for Testing and Materials, Philadelphia, PA (1992).
26. S.J. Zinkle and G.L. Kulcinski, in "The Use of Small-Scale Specimens for Testing Irradiated Material", ASTM STP888; W.R. Corwin and G.E. Lucas, Eds., American Society for Testing and Materials, Philadelphia, PA, 1986, pp. 141-160.
27. S.J. Zinkle and L.T. Gibson, Fusion Semiannual Progress Report, DOE/ER-0313/27, period ending Dec. 31, 1999, pp. 163-174.
28. S.A. Fabritsiev, et al., "Evaluation of Copper Alloys for Fusion Reactor Divertor and First Wall Components", J. Nucl. Mater., 233-237 (1996) 526.